



HAL
open science

A methodology for the 3D characterization of surfaces using X-ray computed tomography: Application to additively manufactured parts

Florian Steinhilber, Joel Lachambre, David Coeurjolly, Jean-Yves Buffiere, Guilhem Martin, Remy Dendievel

► To cite this version:

Florian Steinhilber, Joel Lachambre, David Coeurjolly, Jean-Yves Buffiere, Guilhem Martin, et al.. A methodology for the 3D characterization of surfaces using X-ray computed tomography: Application to additively manufactured parts. *Additive Manufacturing*, 2024, 84, pp.104144. 10.1016/j.addma.2024.104144 . hal-04579719

HAL Id: hal-04579719

<https://hal.science/hal-04579719>

Submitted on 18 May 2024

HAL is a multi-disciplinary open access archive for the deposit and dissemination of scientific research documents, whether they are published or not. The documents may come from teaching and research institutions in France or abroad, or from public or private research centers.

L'archive ouverte pluridisciplinaire **HAL**, est destinée au dépôt et à la diffusion de documents scientifiques de niveau recherche, publiés ou non, émanant des établissements d'enseignement et de recherche français ou étrangers, des laboratoires publics ou privés.



Distributed under a Creative Commons Attribution 4.0 International License

A methodology for the 3D characterization of surfaces using X-ray computed tomography: application to additively manufactured parts

Florian Steinhilber^a, Joel Lachambre^a, David Coeurjolly^b, Jean-Yves Buffiere^a, Guilhem Martin^c, Remy Dendievel^c

^aINSA Lyon, CNRS, MATEIS, Villeurbanne, F-69621, France

^bUniversité de Lyon, CNRS, INSA Lyon, UCBL, LIRIS, Villeurbanne, F-69621, France

^cUniversité Grenoble Alpes, CNRS, Grenoble INP, SIMAP, Grenoble, F-38000, France

Abstract

Many studies highlight the significance of three-dimensional surface topography characterization in assessing its effect on the mechanical or functional properties of materials. This is especially obvious for parts made by additive manufacturing (AM), known for their complex shape and surface topographies. However, a vast majority of 3D characterizations have constraints regarding the macroscopic geometry of the parts they can probe. At the microscale, they are also unable to account for hidden surface features, e.g. notches hidden by unmelted powder particles. Even with the use of X-ray Computed Tomography (XCT) – a tool with the potential to circumvent these issues – data is often reduced to 2D or 2.5D formats for easier analysis, but this leads to a loss of information. This underscores the need for XCT data post-treatment tools to perform thorough 3D surface characterizations. Herein, we introduce a methodology for local roughness and curvature characterization of surfaces of complex shapes using XCT. This method has been designed to be user-friendly, especially for those without extensive data analysis expertise. It provides a comprehensive 3D characterization and efficiently tackles the issues caused by hidden features. After a detailed description of our methodology, we give a first illustrative example based on architected structures fabricated by Electron Powder Bed Fusion (E-PBF). By integrating roughness and curvature metrics, we also derive a parameter indicative of the stress concentrations caused by surface irregularities.

Keywords: 3D surface characterization, X-ray computed tomography, roughness, curvature, additive manufacturing

1. Introduction

Surface topography has a large influence on many functional and mechanical properties of materials. In biomedical applications, implants surface roughness is for instance suspected to have an impact on osseointegration [1, 2] and has been shown to foster bacteria adhesion [3, 4]. For load-bearing structures, surface topography alone may also lead to premature failure if poorly controlled [5, 6]. A rough surface will, for example, have a large area of contact with the environment, possibly accelerating corrosion mechanisms [7]. The presence of surface defects also creates stress concentrations which can lead to crack initiations and thus result in poor fatigue properties [8]. Rough as-built surfaces inherited from additive manufacturing are also more prone to hydrogen embrittlement than polished ones [9]. All these examples emphasize the need for a detailed characterization of surface topography.

In parallel, advancements in material processes are leading to increasingly intricate surfaces. This is particularly the case in Additive Manufacturing (AM), which is gaining considerable attention. Since AM allows greater design freedom, additively manufactured parts often show more complex shapes than those obtained with conventional processes. Architected structures are a typical example [10, 11]. In such cases, standard contact-based roughness instruments or optical systems provide incomplete information due to limited access to the surface. Additionally, at the micro-scale, surfaces inherited from AM exhibit a large variety of surface features, such as notches, unmelted powders, or dross [12, 8, 13]. The interaction between

35 all those surface features can make surface analysis even more challenging. For instance, overhanging surface
 36 features or unmelted powder particles can hide underlying notches, as depicted in Fig.1. This complexity
 37 highlights the need for both instruments and analysis tools that can accurately characterize complex 3D
 38 structures and surface features.

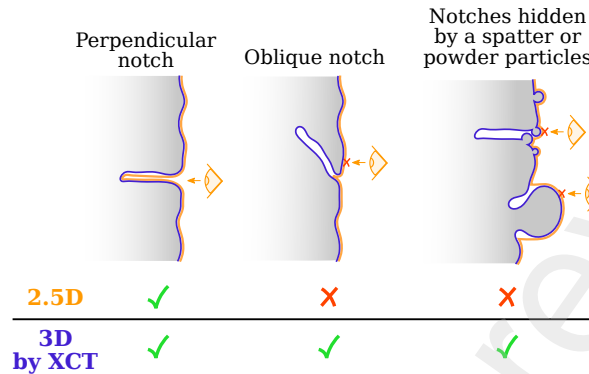


Figure 1: Schematic showing the interest of characterizing AM as-built surfaces in 3D using XCT. Several examples are shown, corresponding to different surface defects. The orange lines show surfaces as seen by a 2.5D characterization tool which probes the surface from a single point of view and without the ability to look through matter. The blue lines correspond to the true surfaces, i.e. the one which would ideally be obtained through XCT using a high resolution, with no noise nor artifacts. In two of the three examples shown, the 2.5D surface characterization fails to account for notches because they are hidden by other surface features.

39 While many studies report 3D roughness analyses, *stricto sensu* most of them are not fully 3D mea-
 40 surements. These approaches have limitations in terms of sample geometry and surface features they can
 41 characterize. These limitations can originate from the instruments used for raw surface acquisition, such
 42 as interferometers or confocal microscopes. The data representation used for subsequent analysis can also
 43 lead to information loss. To clarify this, key concepts will be introduced hereafter to differentiate existing
 44 approaches for 3D surface characterization and their actual capability to characterize complex 3D structures
 45 and surface features.

46 Surface characterization often involves optical instruments like white light interferometry or confocal
 47 microscopy [14, 15, 16, 17, 18]. These instruments use unidirectional light sources, characterizing the surface
 48 from a single perspective. Consequently, surface topography is projected onto a single plane – the one
 49 perpendicular to the light source. This yields height maps with a single z-coordinate value for each (x,y)
 50 point on a regular grid. As the third (z-axis) dimension is only partially used, this data representation can
 51 be referred to as 2.5D [19, 20]. Accordingly, instruments like interferometers or confocal microscopes will be
 52 termed 2.5D instruments hereafter.

53 2.5D characterization is feasible for surfaces with simple geometries like planes or cylinders. For complex
 54 surfaces, irregularities often prevent the measurement tool from accessing certain areas. This is obvious in
 55 AM parts with sophisticated geometries. Even when aiming at characterizing flat and accessible regions,
 56 limitations persist if the surface topography includes hidden features. This effect is depicted in Fig.1. Orange
 57 lines in Fig.1 show that a 2.5D surface characterization manages to describe a notch only if the latter is
 58 perpendicular to the surface. It fails if the notch is oblique or hidden by partially melted powders and/or
 59 spatters.

60 In order to overcome such limitations, developments have recently been made in the field of free-form
 61 metrology [21, 22], which aims at characterizing surfaces of complex and arbitrary shapes. Raw surface
 62 acquisition can now be achieved through instruments like structured light scanners [23, 24] or commercial
 63 X-ray tomographs [25, 26, 16, 20]. These tools offer omnidirectional characterization, thereby facilitating
 64 the characterization of complex surfaces. To fully harness this omnidirectional capability, alternative data
 65 representations are required. The 2.5D representation limits each (x,y) point to only one z-coordinate,
 66 imposing a substantial constraint. To mitigate this, free-form metrology adopts surfaces represented as
 67 meshes or point clouds composed of three-dimensional points (x,y,z). Multiple points with identical x and

68 y coordinates can thus exist.

69 While the free-form surface representation is versatile, it requires novel analysis techniques different from
70 2.5D methodologies, e.g. for surface filtering. Although some studies have employed free-form representa-
71 tions [25, 27, 22, 28], this approach is rarely used. Even when surfaces are captured using methods like
72 XCT, they are often reduced to a 2.5D height map for subsequent analysis [16, 20, 29, 30, 31]. This trend
73 stems from the fact that surface analysis operations, such as filtering of roughness parameters measurement,
74 can be much more complicated when using a complete 3D representation instead of a simpler 2.5D one [21].

75 Thus, some technical issues still need to be overcome to obtain more robust results. Even though the
76 existing solutions may be sufficient, they are often sophisticated and therefore not necessarily user-friendly.
77 They require advanced computer programming skills to be implemented and important computational re-
78 sources. Further work is thus needed to address these challenges and promote the broader adoption of
79 free-form metrology.

80 Another distinction can be made between instruments that are able to look through matter (e.g. XCT)
81 and those that are not (e.g. structured light scanning). Although 3D light scanning enables the charac-
82 terization of complex geometries, it will actually be limited for parts with inaccessible areas (e.g. lattice
83 structures or internal channels) or too complex/small surface features. On the contrary, the ability of XCT
84 to look through matter and have access to internal features enables – at least in theory – the characteri-
85 zation of any shape and account for any hidden surface features. Hence, as depicted by blue lines in Fig.1,
86 XCT succeeds in properly accounting for complex 3D surface features such as notches hidden by unmelted
87 powder, provided that the spatial resolution is sufficiently high.

88 Note that for now, the spatial resolution accessible for each instrument has not been discussed yet.
89 Typically, 2.5D tools achieve superior resolutions compared to XCT, even though recent progress in XCT
90 has made micron-level resolutions feasible using laboratory sources.

91 Tab.1 summarizes the different factors that can influence the capability of the various instruments to
92 properly characterize surfaces with intricate 3D macroscopic shapes and/or hidden microscopic surface
93 features.

	2.5D instruments (e.g. interferometers)	Structured light scanning	XCT
Source directionality	Unidirectional	Omnidirectional	Omnidirectional
Data representation	2.5D	3D possible	3D possible
Ability to look through matter	No	No	Yes
Possible to characterize complex 3D components	No	Yes	Yes
Possible to account for hidden micro-features	No	No	Yes

Table 1: Factors influencing the ability of different instruments to properly characterize surface with complex macroscopic shapes and hidden surface micro-features (e.g. notches hidden by unmelted powder particles).

94 Beyond the question of performing a true 3D surface characterization, it may be important to question
95 which information is the more relevant to extract from it. Most often, roughness characterization is reduced
96 to the analysis of a few roughness parameters that characterize the height distribution of the surface.
97 However, depending on the aim of the study, the surface height distribution may not contain all relevant
98 information. For instance, the stress concentration caused by surface notches is known to be dependent not
99 only on the notch depth (quantified by parameters such as the maximum notch depth S_v) but also on the
100 curvature at its root [32].

101 Hence, various models exist that attempt to predict fatigue life by combining roughness and curvature
102 measurements. Examples include the models of Neuber [33], Arola and Ramulu [34], and Lee et al. [35].
103 Although these models show some conclusive results, they were also found to produce inaccurate estimations
104 in some cases [36, 37]. It is worth noting that they have mostly been applied to regular machined surfaces

105 [38, 39, 40, 37]. Although some recent studies have attempted to extend it to as-built surfaces inherited
106 from AM [35, 41], this area requires further exploration.

107 From a more technical point of view, some improvements could be made to enhance curvature measure-
108 ments and the resulting mechanical prediction accuracy. Many of the studies performed them from 2.5D
109 [42, 40] or 2D [35, 39, 38, 37, 41, 36] data. Such an approach might significantly bias curvature values,
110 similar to the issues observed with roughness measurements. Moreover, when calculating curvature in 2.5D
111 or 3D, various definitions can be considered, e.g. principal, Gaussian, and mean curvature. The choice
112 among these can significantly affect the results. Consequently, it is crucial to select a relevant one based
113 on the intended application. As for now, there is a lack of clear guidance for choosing one definition over
114 another. These issues are an additional motivation for this study.

115 This study introduces a workflow for 3D surface characterization using XCT, measuring both roughness
116 and curvature. By combining these two measurements, we propose a parameter representative of the severity
117 of surface features with respect to mechanical properties. The aim is also to demonstrate the benefit of
118 characterizing surfaces inherited from AM as free-form surfaces, taking into account hidden micro-features
119 and opening new avenues to characterize components showing intricate macroscopic shapes. This approach
120 was designed to be applied to AM samples, but it could also be employed in a broader context, e.g. for as-
121 cast surfaces. An effort was made to ensure its accessibility, i.e. without the need for advanced programming
122 and image analysis skills.

123 For more details about the presented methodology and its application, the reader is redirected to the
124 PhD thesis of Steinhilber [43]. In particular, the methodology is used to study the influence of surface
125 roughness on fatigue properties of Ti64 samples produced by Electron beam Powder Bed Fusion (E-PBF)
126 and Laser Powder Bed Fusion (L-PBF).

127 2. Materials and XCT data acquisition

128 Different samples were used to demonstrate the application of the developed workflow. All were man-
129 ufactured by Electron Powder Bed Fusion (E-PBF) using an ARCAM A1 machine and Ti64 powders. To
130 characterize their as-built surface, no surface treatment was applied. Powder grain size distribution ranged
131 from 60 μm to 100 μm and the layer thickness was set to 50 μm . More details about the processing conditions
132 can be found in [8]. To characterize their surface, samples were scanned using laboratory XCT.

133 A 2 mm vertically built cylinder was first used as a first simple example. It was scanned using a cone beam
134 phoenix | x-ray V | tome | x laboratory tomograph with a voltage of 90 kV, a current of 240 μA , an exposure
135 time of 333 ms and 720 projections. No physical filter was used during the scan acquisition. Reconstruction
136 was performed using a standard filtered back projection algorithm (phoenix datos x software). The voxel
137 size used was 2.5 μm , but volumes were downscaled by a factor 2 before further analysis¹. The resulting
138 voxel size is therefore 5 μm .

139 Two as-built Ti64 architected structures were also characterized: a gyroid structure [45, 46, 11] and an
140 octet-truss lattice structure, see Fig.2.

141 XCT scans were made with an RX Solutions laboratory tomograph using a Cu filter to mitigate beam
142 hardening artifacts. The main acquisition parameters are summarized in Tab.2. Two scans were acquired
143 at different resolutions for the gyroid structure. For all architected structures, reconstructions were done
144 using an implementation of FDK algorithm [47].

145 All XCT scans were converted to 8-bit after reconstruction to reduce data size. After conversion, volumes
146 size were 158 Mo, 4.6 Go and 5.1 Go for the cylinder, the gyroid (10 μm scan) and the octet-truss lattice
147 respectively.

¹The data were retrieved from the work of Persenot [44], who performed this downscaling to reduce data size.

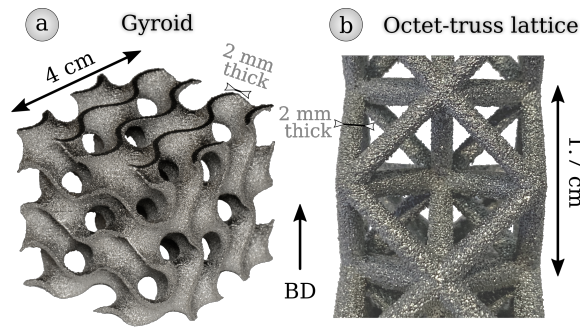


Figure 2: Ti64 architected structures fabricated by E-PBF. (a) Gyroid structure. (b) Octet-truss lattice structure.

Sample	Gyroid	Gyroid	Octet truss
Voxel size (μm)	5	10	10
V (kV)	230	230	230
I (μA)	35	70	58
Cu Filter (mm)	1.4	1	1
Number of projections	3616	3616	2240
Exposure time (ms)	2000	333	500

Table 2: Acquisition parameters for XCT scans performed using the RX Solutions laboratory tomograph.

148 3. 3D surface characterization methodology

149 3.1. Surface segmentation

150 The first step of surface characterization is the segmentation, i.e. the extraction of the surface from XCT
 151 scans. Since it can be affected by noise, a noise-reducing filter is applied to the reconstructed volume before
 152 further calculations. An edge-preserving filter is used to preserve a detailed description of the surface [48].
 153 A median filter is used because it provides satisfying results while keeping computing time reasonable for
 154 large volumes.

155 After filtering, the sample is segmented from the volume through thresholding. Here, thresholding aims
 156 at separating the two main peaks of the grayscale histogram, which will be referred to as dark (voids) and
 157 bright (sample) peaks – see Fig.3a. Several methods can be used to automatically determine an optimal
 158 threshold. One of the most popular is Otsu's method [49, 50]. The latter makes the assumption that all
 159 voxels are separated into two classes based on their gray level while minimizing the inter-class variance. It
 160 yields in most cases consistent and robust results.

161 However, it may not always be the best choice if one is looking for some specific surface features such as
 162 surface defects that will be prone to initiate failure during mechanical loading. In this specific case, partially
 163 melted particles are unlikely to be of much interest. They can even hide more severe surface defects such
 164 as notches. Contrariwise, deep and sharp notches are very often the most critical defects and are therefore
 165 of great interest. However, the sharpest ones are often difficult to segment from XCT data, because the
 166 corresponding voxels show intermediate grayscale values. This leads Otsu's method to consider many of
 167 them as foreground voxels, erasing notches from the surface although they are the most interesting defects
 168 when questions related to crack initiation and failure must be tackled.

169 This effect can be seen in Fig.3b and Fig.3c. Fig.3b shows an XCT radial slice of a 2 mm as-built E-PBF
 170 cylinder, where two deep notches can be seen. Fig.3c shows in orange the pixels considered as foreground

171 using Otsu's threshold for segmentation. It can be seen that both notches are not properly accounted for
 172 when using Otsu's threshold, although they are clearly visible on the grayscale image in Fig.3b.

173 A threshold corresponding to a higher grayscale value than Otsu's one will be certainly more adapted to
 174 capture such severe surface defects. Indeed, both partially melted particles and sharp notches typically show
 175 intermediate grayscale values because they are at the interface between matter and air. Thus, selecting a
 176 threshold that stands at the end of the plateau – just at the left border of the histogram's bright peak –
 177 will enable to discard some parts of unmelted powder particles while better capturing sharp notches.

178 The thresholding method proposed is inspired by the triangle threshold introduced by Zack et al. [51]. It
 179 is thereafter referred to as the Triangle Threshold for Bimodal Histograms (TTBH). Its principle is described
 180 schematically in Fig.3a.

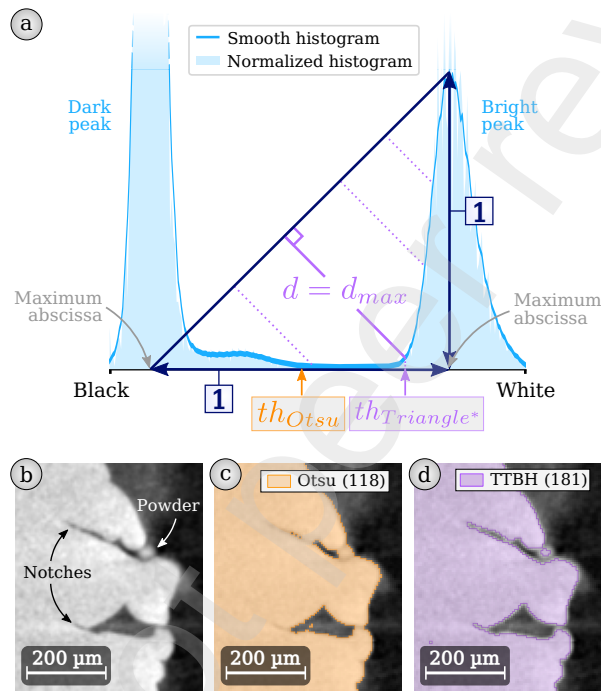


Figure 3: (a) Definition of the TTBH, illustrated based on the E-PBF cylinder normalized grayscale histogram. (b) XCT 8-bit radial slice showing two sharp notches and a partially melted powder (voxel size = 5 μm). (c) Otsu's threshold application (orange area) (d) TTBH application (purple area).

181 First, if the histogram is too noisy, it may be useful to smooth it. In the present work, a moving average
 182 of size 10 is applied. Second, the histogram is normalized so that both the bright peak maximum and the
 183 distance between the two histogram peaks are equal to 1. Finally, the desired threshold is simply the gray
 184 value which maximizes the distance d as defined in Fig.3a. As required, the obtained threshold is located
 185 just at the left edge of the bright peak. Fig.3d shows that the two sharp notches are clearly better captured
 186 using the TTBH than by Otsu's method. The powder grain is cropped, which can be both an advantage
 187 and a drawback, depending on which surface features one aims to characterize.

188 It may be worth mentioning that this thresholding method is particularly sensitive to noise and artifacts
 189 (e.g. beam hardening). This can be at least partially compensated by the use of the proper noise-reducing
 190 filter beforehand. It may also be relevant in some cases to make a compromise between the TTBH and
 191 Otsu's threshold. A simple and convenient way to do that can be to calculate both and take an intermediate
 192 value.

193 Following segmentation, the volume undergoes a cleaning process to remove all internal pores or tiny
 194 objects caused by measurement noise. This cleaned binary volume is subsequently referred to as the sample
 195 mask, illustrated in Fig.4b. In our case, the sample surface is defined as the surface mask depicted in

196 Fig.4c. It is the binary mask whose foreground is composed of all surface voxels. These surface voxels are
 197 the foreground voxels of the sample mask which have at least one background voxel as first neighbor. A
 198 connectivity of 1 is used to determine neighbors.

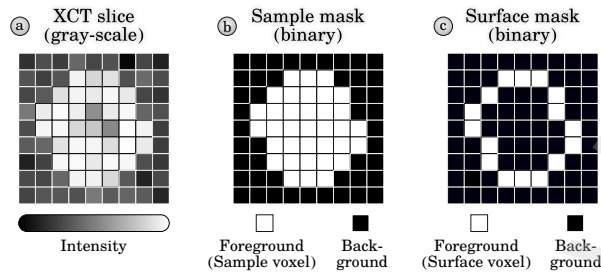


Figure 4: (a) Schematic example of a grayscale XCT slice. (b) Corresponding sample mask. (c) Corresponding surface mask.

199 3.2. 3D roughness calculation

200 The topography of a surface is often divided into 4 components, each one corresponding as a first ap-
 201 proximation to a range of spatial frequencies: the object's form, the waviness, the roughness, and the
 202 micro-roughness [52, 53]. Most commonly, only the roughness component is considered significant for char-
 203 acterizing surface micro-features such as notches or unmelted powder particles. The form and waviness
 204 typically represent geometric deviations, while micro-roughness is often viewed as measurement noise. The
 205 objective is therefore to discriminate roughness from these other components to achieve a complete surface
 206 characterization.

207 In the case of a conventional 2.5D surface characterization, the shape of the characterized surface is
 208 necessarily simple (plane, cylinder...). Form removal, which consists of subtracting the component geometry,
 209 can thus be done rather easily using least-squares optimization. Filters are then used to discriminate
 210 roughness from waviness (L-filter) and micro-roughness (S-filter). In both cases, the Gaussian filter is the
 211 default option [53].

212 However, 2.5D characterization is only possible for parts with simple geometry, as discussed in Section
 213 1. In order to take full advantage of XCT, a 3D surface representation must be used – e.g. a mesh or a
 214 point cloud made of points with arbitrary (x,y,z) coordinates. In this case, the roughness characterization
 215 workflow can be more challenging. In particular, the form removal step is complex when no analytical
 216 expression is adapted. For 3D printed parts, a first approach consists of using the CAD file as a reference.
 217 This is sometimes done to measure geometrical deviations between the manufactured part and its CAD
 218 model [54, 55, 29, 56]. However, this requires the CAD file to be available, and the geometrical deviations
 219 to be small enough to get an accurate measurement.

220 If the CAD file cannot be used, it is possible to smooth the raw surface and use the result as a reference.
 221 In this case, the roughness is defined as the distance between the surface and a smoothed version of it. A
 222 number of studies already addressed this topic, see the work of Jiang and Scott [21] for an extensive review.
 223 In such studies, surfaces are generally meshed and may be smoothed using morphological filters [57, 25],
 224 diffusion-based filters [58], anisotropic diffusion-based filters [59], or wavelet decomposition [60].

225 The methodology presented here follows the same principle of surface smoothing and distance measure-
 226 ment. It can thus be applied to complex geometries without any need for a prior knowledge. However, unlike
 227 most common processing workflows, in our case, the surface is not extracted as a mesh for calculations. In-
 228 stead, all calculations are done on the digital volume obtained by XCT. One of the advantages is that it
 229 can be implemented in standard open-source image analysis software such as ImageJ. The overall image
 230 analysis workflow is schematically illustrated in Fig.5. An example of implementation of such a workflow
 231 using ImageJ can also be accessed via the online repository [61].

232 The proposed workflow only uses as input data the sample mask, whose computation is detailed in
 233 Section 3.1.

234 The first step is the computation of the surface mask – also defined in Section 3.1. The latter will be
 235 used at the end of the workflow to extract data from volumes only at the voxels of interest – i.e. the surface
 236 voxels. The surface mask can be obtained by applying an erosion to the sample mask, and then computing
 237 the logical XOR operation between the sample mask and the result of the erosion.

238 The second step of the workflow is the smoothing step. It is done here by converting the sample mask to
 239 float or integer values and applying a 3D Gaussian filter². The chosen degree of smoothing will determine

²An alternative solution, not developed here, would be to perform smoothing by applying a 3D morphological filter [62, 21] on the sample mask.

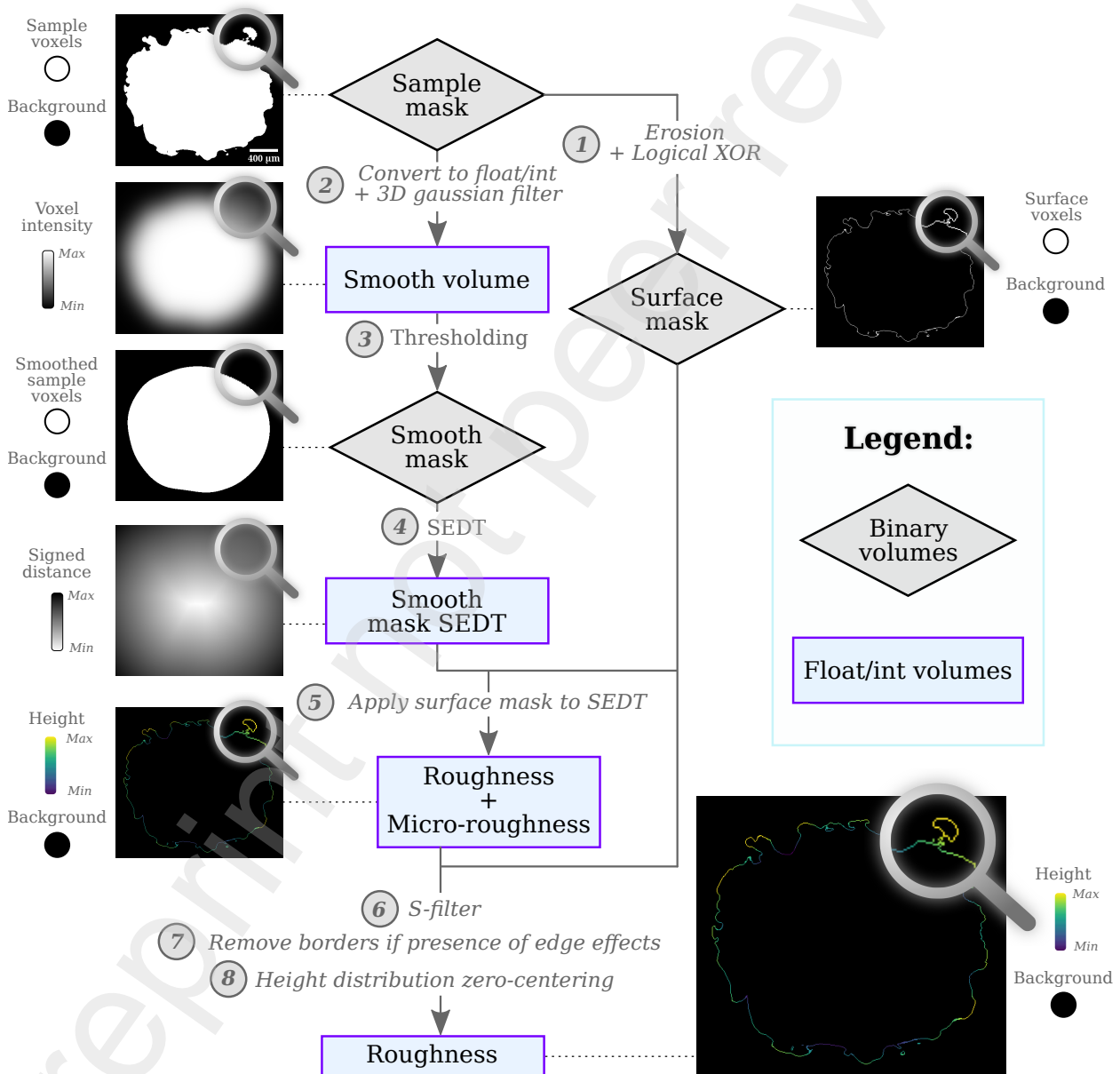


Figure 5: Workflow proposed for the 3D roughness computation. The sample mask and surface mask are defined in Fig.4. The images shown correspond to transverse cross-sections of a 2 mm E-PBF Ti64 cylinder at different steps of the calculation.

240 the limit between roughness on the one hand and waviness/form on the other hand. It is quantified by
241 the cut-off wavelength λ_c [63], which is the wavelength considered to discriminate form and waviness from
242 roughness. From an image processing point of view, a Gaussian filter is more often adjusted using the
243 standard deviation σ , which can be easily derived from the cut-off wavelength following Eq.1.

$$\sigma = \sqrt{\frac{\ln 2}{2}} \cdot \frac{\lambda_c}{\pi} \approx 0.187 \cdot \lambda_c \quad (1)$$

244 where σ and λ_c are the standard deviation and the cut-off wavelength of the Gaussian filter respectively.

245 ISO standards provide rules to appropriately set the value of the parameter λ_c [53]. Although they are
246 meant for 2D filters applied to height maps, they are used by extension in the developed workflow to adjust
247 the 3D Gaussian filter. Ideally, the choice should be made by observing the surface and identifying the
248 features that need to be characterized as roughness. It is then advised to set λ_c to be five times the size
249 of the largest feature of interest, choosing among a list of predetermined values (0.25 mm, 0.8 mm, 2.5 mm,
250 etc.) [53]. This choice is somehow arbitrary, especially for surfaces obtained by AM with complex topologies.
251 This can explain the large variations of values used in the literature on AM materials [64]. Grazia Guerra
252 and Lavecchia [27] used for example a cut-off wavelength of 0.25 mm while Vetterli et al. [65] used several
253 values up to 2 mm.

254 In the third step of the workflow, the smoothed volume obtained after filtering is segmented by thresh-
255 olding. This results in a smoothed version of the sample mask, hereafter referred to as the smooth mask.
256 The latter is then used as reference for roughness calculation. The most straightforward choice for the
257 threshold value is the mean of background and foreground voxels values (e.g. 127.5, if the background is
258 0 and foreground voxels are 255). However, this leads in general to some volume shrinkage, especially for
259 large λ_c values. To avoid this problem, the threshold value is instead determined automatically so that the
260 smooth mask volume equals the volume of the original mask.

261 The fourth step aims at computing the distance between the sample surface and its smoothed version. For
262 this purpose, the Signed Euclidean Distance Transform (SEDT) is computed from the smooth mask. This
263 results in a float volume where the value at each foreground voxel is the distance to the nearest background
264 voxel, and contrariwise for the values at the background voxels. The distances are signed, e.g. positive for
265 background voxels and negative for foreground voxels.

266 At the fifth step, the surface mask is applied to the smooth mask SEDT. This results in a sparse volume
267 where most of the voxels have the same background value (e.g. 0), except the surface voxels which hold the
268 distances to the smooth mask, i.e. the sought roughness values.

269 The sixth step consists in applying an S-filter. This aims at removing the highest frequencies, in other
270 words, the micro-roughness. The standard filter used for this purpose is again a Gaussian filter [53]. The
271 cut-off wavelength used for this filter is commonly denoted λ_S . A procedure to calculate the S-filter using 3D
272 Gaussian filters only based on normalized convolution [66] is described in Appendix A. This filtering step
273 becomes particularly relevant if the voxel size set for XCT scans is not small enough to properly describe the
274 surface topography. When the voxel size approaches the dimensions of surface features, the surface tends
275 to be oversimplified and discretized, yielding a staircase appearance. Such oversimplification can result in
276 sharp fluctuations in the roughness measurement. Using the S-filter helps to moderate such abrupt changes.

277 The seventh step addresses edge effects that arise due to Gaussian filtering [67]. When computing the
278 filtered value for a particular voxel using the Gaussian kernel, surrounding voxels are taken into account.
279 However, for those voxels near the XCT scan boundary, the convolution radius might extend past this
280 boundary. For these voxels, the XCT scan has to be extrapolated, for instance using an arbitrary constant
281 value. The most common choice is zero. This value aligns well with our needs since 0 represents the
282 background value that is assumed to envelop the sample. However, this method can result in biased values
283 for surface voxels too close to the scan boundary. For example, in the context of a cylinder scan, the topmost
284 and bottommost surface voxels may contain such biased values.

285 Various solutions have been suggested to address this challenge for 2D or 2.5D roughness measurements
286 [68]. The most straightforward solution is to discard roughness values for points located too close to the
287 edges, typically within a distance of the cut-off value or half of it. In the described workflow, the approach

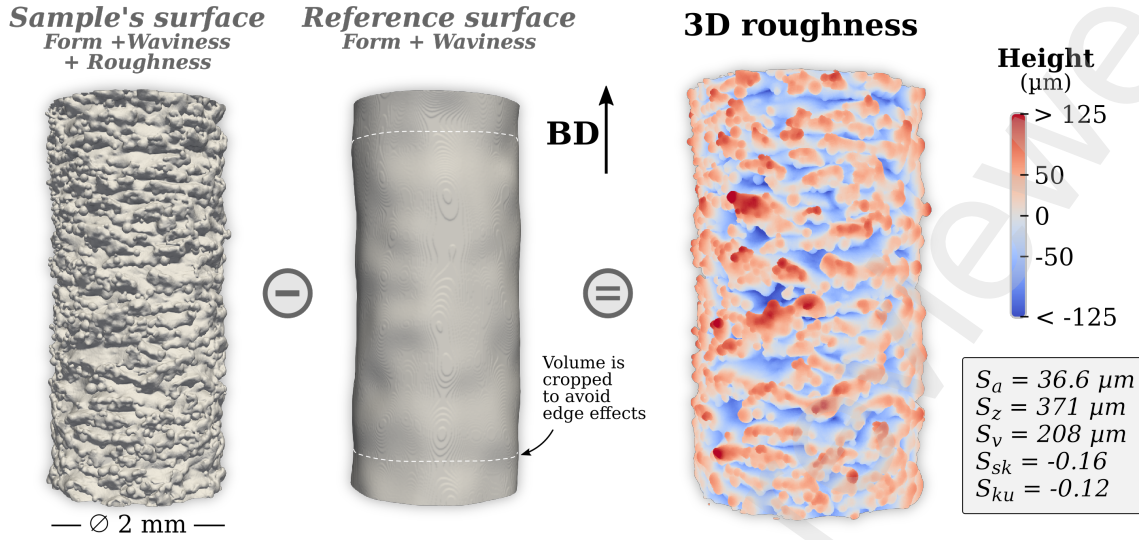


Figure 6: Surface roughness measurements, as described in Fig.5, applied to a 2 mm diameter as-built E-PBF cylinder. Computations were made from an XCT scan with a voxel size of $5 \mu\text{m}$. Cut-off values were set to $\lambda_c = 0.8 \text{ mm}$ and $\lambda_s = 0.015 \text{ mm} = 3 \text{ voxels}$. To avoid edge effects, points closer to the boundaries than $\frac{\lambda_c}{2}$ were discarded. Formulas for roughness parameter computations are given in the ImageJ and Python scripts in an online repository [61].

288 adopted involves cropping the upper and lower borders by a width of $\frac{\lambda_c}{2}$ wherever necessary. However, if
 289 this method results in discarding too much data, other strategies, based on extrapolation or the use of
 290 normalized convolution [66], can be employed in the Gaussian filtering step. This would allow the user to
 291 address edge effects without the need to truncate volumes later on.

292 Lastly, the eighth step ensures that the height distribution is zero-centered, meaning the average height
 293 is zero. This condition is intuitive and is assumed when computing certain roughness parameters like S_{sk}
 294 and S_{ku} . To achieve this, the average height is subtracted from the height of each surface voxel.

295 An example of roughness calculated on a 2 mm diameter cylinder fabricated by E-PBF is shown in
 296 Fig.6. The initial sample's surface and the smooth reference surface are displayed, as well as the derived
 297 roughness. Note that points closer than $\frac{\lambda_c}{2}$ to the upper and lower boundaries were discarded at the end of
 298 the computation.

299 The triangle threshold for bimodal histograms presented in Section 3.1 was used for surface segmentation
 300 and a cut-off wavelength λ_c of 0.8 mm has been chosen for roughness calculation. Regarding the S-filter cut-
 301 off λ_s , a value of three times the voxel size (0.015 mm) was used.

302 As far as computational performance is concerned, the use of 3D operations makes the presented method-
 303 ology demanding in terms of Random Access Memory (RAM). This can be a limitation for large volumes,
 304 which can be overcome to a certain extent by dividing the volume and performing computations in several
 305 steps. Processing time is nonetheless reasonably low since efficient implementations exist for the operations
 306 used. As an example, the computation for the 158 Mo XCT scan of the cylinder in Fig.6 took around 1 min
 307 on a conventional laptop with 8 CPU cores and using the ImageJ macro that can be accessed via the online
 308 repository [61]. A Python implementation is also given in [61], with some improvements to limit RAM usage
 309 and significantly increase computation speed.

310 3.3. 3D curvature calculation

311 The curvature κ is a measure of how a curve (in 2D) or a surface (in 3D) bends at a particular point.
 312 For a curve, it corresponds to the inverse of the radius ρ of the osculating circle at this given point, as
 313 schematically shown in Fig.7a.

314 Curvature is a more complex concept for surfaces and several definitions exist. The closest 3D equivalent
 315 of the curvature in 2D would be the directional curvature, which measures how much the surface bends along

316 a particular direction. When the surface bends outward, the directional curvature is positive; conversely,
 317 it is negative. This requires a prior definition of which side of the surface is considered to be the outside.
 318 Although directional curvature can be calculated in an infinite number of directions, two are of particular
 319 interest. These are the direction of minimum curvature \vec{d}_{min} and the one of maximum curvature \vec{d}_{max} (the
 320 sign being considered), also known as principal directions. The corresponding curvatures are called the
 321 principal curvatures κ_{min} and κ_{max} .

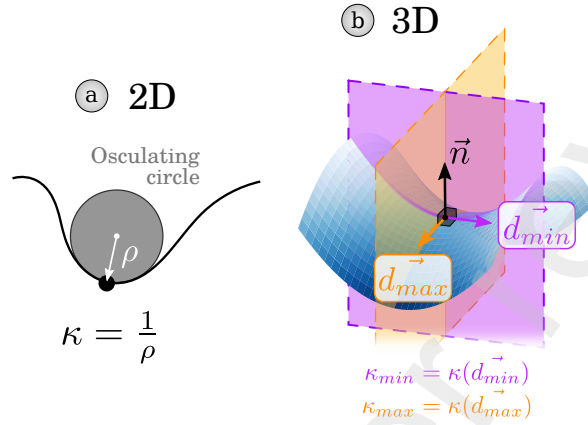


Figure 7: (a) Definition of the curvature κ and the radius of curvature ρ for a curve in 2D. (b) Schematic representation of a saddle-like surface. The normal \vec{n} and the principal directions are indicated at the saddle point. In this particular case, $\kappa_{min} < 0$ and $\kappa_{max} > 0$.

322 Fig.7b shows an example of a saddle-type surface, where \vec{d}_{min} and \vec{d}_{max} are respectively displayed in purple
 323 and orange.

324 Knowing principal directions and curvatures, the directional curvature in any direction can be derived
 325 using Eq.2 [69].

$$\kappa(\vec{v}) = \begin{pmatrix} v_n \\ v_{min} \\ v_{max} \end{pmatrix}^\top \cdot \begin{pmatrix} 0 & 0 & 0 \\ 0 & \kappa_{min} & 0 \\ 0 & 0 & \kappa_{max} \end{pmatrix} \cdot \begin{pmatrix} v_n \\ v_{min} \\ v_{max} \end{pmatrix} \quad (2)$$

$$= v_{min}^2 \cdot \kappa_{min} + v_{max}^2 \cdot \kappa_{max}$$

326 where $\kappa(\vec{v})$ is the directional curvature in the direction \vec{v} , $\vec{v} = v_n \cdot \vec{n} + v_{min} \cdot \vec{d}_{min} + v_{max} \cdot \vec{d}_{max}$ is an arbitrary
 327 vector and $\vec{n} = \vec{d}_{min} \times \vec{d}_{max}$ is the surface normal.

328 Finally, two other common curvatures are often used: the mean curvature κ_{mean} and the Gaussian cur-
 329 vature κ_{gauss} (see definitions in Eq.3 and Eq.4).

$$\kappa_{mean} = \frac{\kappa_{min} + \kappa_{max}}{2} \quad (3)$$

$$\kappa_{gauss} = \kappa_{min} \cdot \kappa_{max} \quad (4)$$

330 Although exact curvatures may be derived for parametric surfaces defined by analytical formulas, only
 331 estimations are possible for digital surfaces such as the one obtained by XCT. Several techniques can be
 332 used for this purpose. Point clouds can for example be approximated locally by a quadratic surface, which
 333 enables to derive curvature estimates from the obtained analytical formula [70].

334 For surfaces defined as the boundary of a collection of voxels in 3D, integral invariants-based estimators
 335 have demonstrated their interests both in terms of accuracy and efficiency [71]. The principle is to move a
 336 spherical convolution kernel of radius r_{curv} along the surface – see Fig.8 for an example in 2D. Its intersection
 337 with the volume enables the estimation of some differential geometrical quantities.

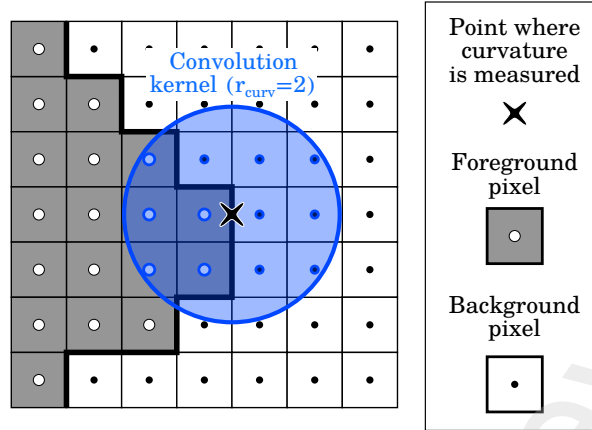


Figure 8: Principle of integral invariant based curvature measurement from a digital shape. The example is given in 2D for clarity, but the principle remains the same for volumes. Here, the intersection area between the convolution kernel and the object is measured by counting the number of pixels whose center falls into the kernel of radius r_{curv} .

338 For example, κ_{mean} is directly related to the volume of the intersection between the convolution kernel
 339 and the object. Hence, an estimation of κ_{mean} at a given boundary point can be computed using Eq.5 [72].

$$\kappa_{mean}(r_{curv}) = \frac{16}{3 \cdot r_{curv}} \cdot \left(\frac{1}{2} - \frac{V_{inter}(r_{curv})}{\frac{4}{3} \cdot \pi \cdot r_{curv}^3} \right) \quad (5)$$

340 where r_{curv} is the radius of the spherical convolution kernel and $V_{inter}(r_{curv})$ is the portion of the convolution
 341 kernel's volume that resides inside the surface's boundary. By computing the covariance matrix of the
 342 intersection instead of its volume, it is possible to design estimators for the complete curvature tensor and
 343 thus estimate likewise principal curvatures and directions [71].

344 Since computations are made on volumes, this offers the opportunity to perform computations using
 345 software such as ImageJ. Using Eq.5, κ_{mean} can for instance be computed using a linear convolution. Since
 346 an optimized implementation of this method is already available in the open-source C++ library DGtal, it
 347 has been used in the present work [73].

348 The only parameter needed to perform the calculation is the radius of the convolution kernel r_{curv} , which
 349 is the scale at which the curvature is computed. Although this parameter is of great importance and has
 350 a quite intuitive meaning, it can be difficult to properly set in practice. A first constraint that limits the
 351 possible values for r_{curv} is the resolution of the XCT scan, since a minimum of a few voxels are necessary
 352 to limit noise in the measured curvature. If one aims at minimizing the noise while keeping the curvature
 353 measurement at a fine scale, it was found useful to apply a denoising filter after curvature computation. For
 354 this purpose, we used the same Gaussian filter that was used for the S-filter in Section 3.2.

355 The choice of the convolution radius can also be driven by physical considerations and depends on the
 356 scale of the surface features of interest. This is the case in the example shown in Section 3.2, where curvature
 357 at a large scale can be used to detect biased roughness measurements near sharp geometrical features.

358 The various definitions of curvatures introduced previously are complementary because they carry dif-
 359 ferent information, see e.g. Fig.9. Depending on the objective, one definition can be more relevant than
 360 others. Mean curvature is for example a relevant parameter concerning surface tension and wetting issues
 361 [74]. Triply Periodic Minimal Surfaces (TPMS) such as gyroids, which can be manufactured using AM
 362 processes [75, 76, 77, 78], are also characterized by a zero mean curvature. Such structures were for example
 363 found to achieve interesting energy absorption properties [79]. Gaussian curvature provides complementary
 364 information. For instance, a surface characterized by a zero Gaussian curvature is a developable surface
 365 (e.g. a cylinder). In the present work, curvature is computed with the aim to characterize surface notches
 366 and distinguish them from other surface features. The maximum and Gaussian curvatures do not seem to

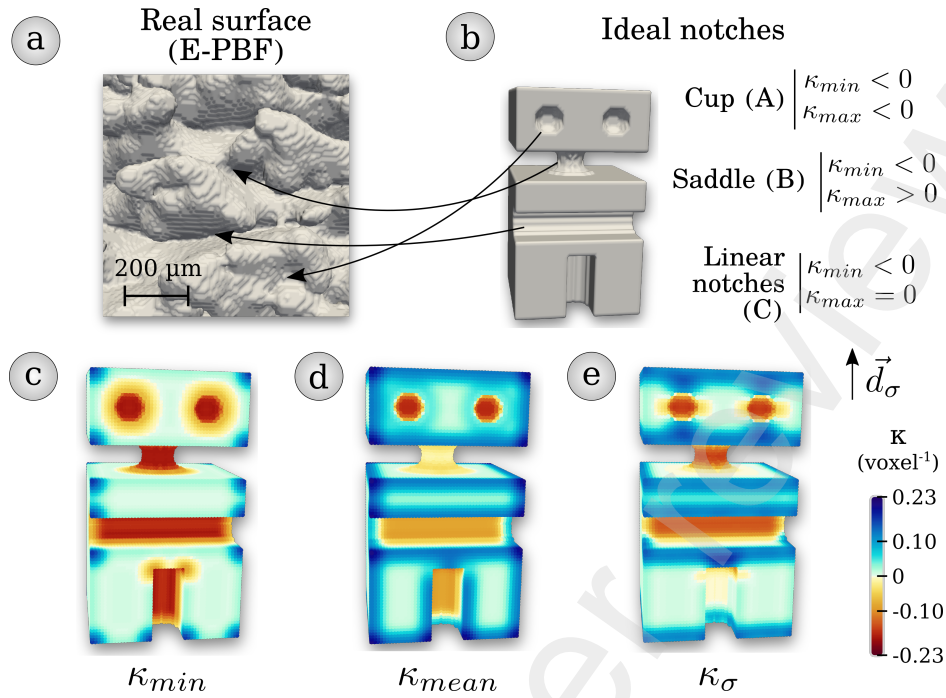


Figure 9: Guide for the choice of relevant curvatures for the characterization of notches. (a) Notches visible on a surface mesh extracted from an XCT scan of an as-built surface inherited from E-PBF. (b) Artificial object used as model, with different types of notches. Each notch present in the artificial object shows a configuration that can be found on a real surface. (c) κ_{min} , (d) κ_{mean} , and (e) κ_{σ} measurements on the artificial object. κ_{σ} is here computed assuming that \vec{d}_{σ} is vertical. Notch roots have by definition a radius of curvature of 5 voxels (i.e. $\kappa = 0.2$).

367 be suited for this purpose, as they will have the same value (zero) both on a perfectly flat surface without
 368 any notch and at the root of a linear notch in a plane.

369 The choice between the other curvatures being less straightforward, Fig.9 is helpful to guide our final
 370 choice. Fig.9b displays an artificial object showing ideal notches with different geometries. Each of those
 371 notches represents a configuration that can be found locally on a real surface, see Fig.9a. Notches A are cups,
 372 i.e. areas where $\kappa_{min} < 0$ and $\kappa_{max} < 0$. Notch B exhibits a saddle-like geometry, with principal curvatures of
 373 opposite signs. Notches C are linear ones in a plane, i.e. $\kappa_{min} < 0$ and $\kappa_{max} = 0$. Two orientations are shown
 374 to demonstrate that it is possible to discriminate different notches based on their orientation.

375 Three curvatures are computed on this artificial object, namely κ_{min} , κ_{mean} and κ_{σ} . $\kappa_{\sigma} = \kappa(\vec{d}_{\sigma})$ is the
 376 directional curvature along the direction \vec{d}_{σ} (vertical in this case). The comparison of the three curvatures
 377 in Fig.9c-e makes it possible to identify which one highlights best the different notches.

378 The first one is the minimum curvature κ_{min} , which successfully captures all notches. Furthermore, all
 379 have the same κ_{min} value. The second curvature is κ_{mean} . Cups (type A) have the lowest κ_{mean} value whereas
 380 linear notches (C) show intermediate values. This difference is not necessarily desirable, since cups are not
 381 expected to reduce the mechanical properties more than linear notches. Even worse, κ_{mean} tends to 0 for the
 382 saddle-like notch (B). Although this notch was chosen as an example for the sake of clarity and seems far
 383 from a real case, there are many regions of the surface where $\kappa_{min} < 0$ and $\kappa_{max} < 0$. Thus, κ_{mean} seems less
 384 relevant than κ_{min} to detect notches in general because it is somehow biased by the κ_{max} contribution.

385 Finally, the third curvature is the directional one, κ_{σ} . As illustrated in Fig.9e, all notches are well
 386 identified except the one parallel to \vec{d}_{σ} . High κ_{σ} values are also more concentrated at notches roots in
 387 comparison with κ_{min} . κ_{σ} can thus be considered the most appropriate choice when one aims at characterizing
 388 surface features with a specific orientation with respect to a loading direction.

389 Based on these considerations, both κ_{min} and κ_{σ} were thus computed on the same cylindrical sample used

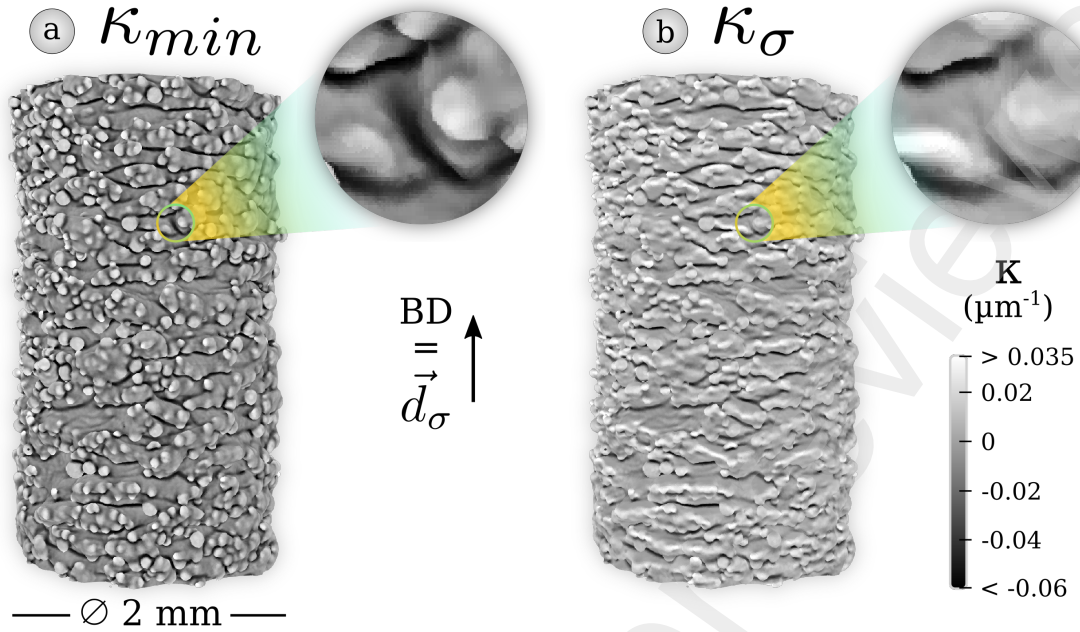


Figure 10: (a) κ_{min} and (b) κ_{σ} measurements on an as-built cylindrical sample fabricated by E-PBF. Computations were made from an XCT scan with a voxel size of $5\ \mu\text{m}$, using $r_{curv} = 30\ \mu\text{m} = 6\ \text{voxels}$ and $\lambda_S = 0.025\ \text{mm} = 5\ \text{voxels}$. The magnifying windows provide an enlarged view on a notch parallel to \vec{d}_{σ} . It shows that κ_{σ} manages to ignore it, whereas notches perpendicular to the loading direction are kept.

390 in Section 3.2, see Fig.10a-b. Since the sample is a fatigue specimen meant to be loaded along its axis, κ_{σ} was
 391 computed along this direction. A radius of $30\ \mu\text{m}$ ($= 6\ \text{voxels}$) was chosen here for the convolution kernel.
 392 An additional filter was used similarly to what has been done for roughness, using $\lambda_S = 0.025\ \text{mm} = 5\ \text{voxels}$.
 393 These choices were made to provide a sufficiently detailed curvature measurement without being too much
 394 affected by noise. Fig.10a shows that κ_{min} underlines the presence of notches, which correspond to the lowest
 395 values. κ_{σ} greatly attenuates the vertical notches, which can be seen when comparing enlarged views in
 396 Fig.10a and Fig.10b.

397 3.4. Quantification of the harmfulness of surface notches

398 The objective here is to combine both roughness and curvature to derive a parameter accounting for the
 399 mechanical severity of surface features. For surfaces derived from AM, the surface features that are expected
 400 to have the most significant impact on mechanical properties are notches [80, 8, 81]. To account for this
 401 notch effect, the simple analytical formula given in Eq.6 is used. It gives the stress concentration factor at
 402 the root of an elliptical notch in a semi-infinite panel, in the absence of plastic deformation [32]. The two
 403 parameters required to estimate the stress concentration factor K_t are the notch depth d and the radius of
 404 curvature at its root ρ (see Fig.11).

$$K_t = 1 + 2\sqrt{\frac{d}{\rho}} \quad (6)$$

405 In the previous sections, d is estimated by the local height, which corresponds to roughness, while ρ was
 406 defined by the inverse of the curvature κ_{σ} . Some approximations still have to be made to apply Eq.6 using
 407 those parameters.

408 First, it is important to emphasize that both the roughness and curvature, as calculated in Section 3.2
 409 and 3.3, are estimates. Therefore, their values may depend on the method and parameters used for their
 410 measurement. The curvature values, for instance, are notably influenced by changes in the convolution

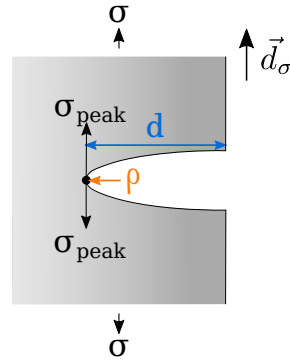


Figure 11: Elliptical notch in a semi-infinite panel, submitted to a tensile stress σ in the direction \vec{d}_σ perpendicular to the ellipse major axis. d and ρ are respectively the depth of the notch and the radius of curvature at its root. This notch generates a stress concentration given by Eq.6, which means that the local stress at its root σ_{peak} is higher than the nominal stress in the section.

411 radius r_{curv} and in the voxel size. While there are theoretical proofs, such as the one presented by Coeurjolly
 412 et al. [72], showing that integral invariant-based calculations approach exact curvature values as voxel size
 413 reduces, the resolution required to observe this might be very high. Keeping this in mind, one should treat
 414 these estimated values as semi-quantitative ones, that can for instance be used for ranking the severity of
 415 notches.

416 Another approximation to consider is that Eq.6 is valid at the notch tip, which might be hard to detect
 417 automatically. As a result, the formula has been generalized and applied to every point on the surface where

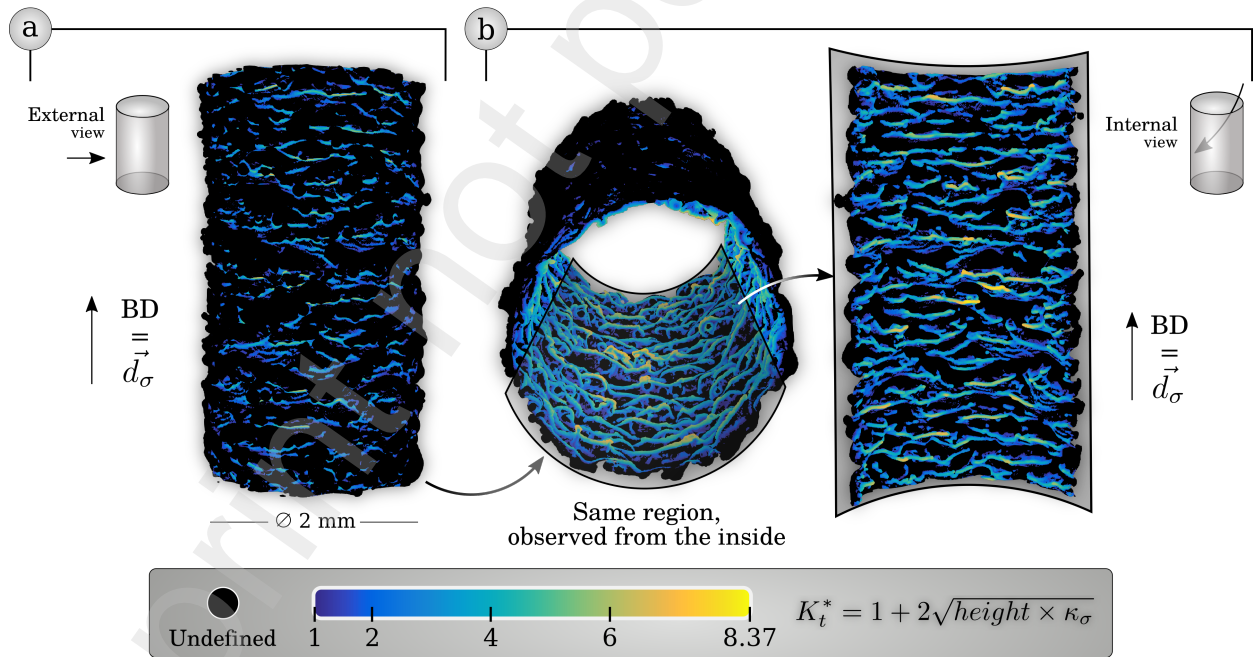


Figure 12: K_t^* maps of a 2 mm diameter cylindrical sample fabricated by E-PBF. The K_t^* formula is given in Eq.7 and makes use of the roughness and curvature measured in the previous sections. The curvature κ_σ is computed in the direction of the cylinder axis, which also corresponds to the build direction. The points where K_t^* is not defined – because $d \geq 0$ or $height \geq 0$ – are by default colored in black. The parameters used for computations are $\lambda_c = 0.8 \text{ mm}$ | $\lambda_S = 0.015 \text{ mm}$ for roughness, and $r_{curv} = 50 \mu\text{m}$ | $\lambda_S = 0.025 \text{ mm}$ for curvature. (a) Surface as seen from the exterior of the sample. (b) Surface as seen from the interior of the sample. The internal point of view is obtained from the surface extracted from the XCT scan.

418 both $\kappa_\sigma < 0$ and $d < 0$. This means it is used across the entire notches, not just at their root. While Eq.6
 419 might not be applicable for numerous points, the highest values will still be found at the notch roots where
 420 the depth is maximal and the curvature is minimal. Therefore, the values derived are still relevant, especially
 421 when identifying areas with the highest stress concentration. In other words, it provides a semi-quantitative
 422 parameter that reflects the mechanical severity of surface notches. Finally, an approximate value of K_t ,
 423 called K_t^* , can be computed at the sample surface using Eq.7.

$$K_t^* = 1 + 2 \sqrt{\text{height} \cdot \kappa_\sigma} \text{ where } \text{height} < 0, \kappa_\sigma < 0 \quad (7)$$

424 where K_t^* is the estimated local stress concentration, *height* is the local surface height obtained from roughness
 425 measurements and κ_σ is the directional curvature along the loading direction.

426 Fig.12 shows an example of a K_t^* map computed from the same cylindrical sample used in the previous
 427 sections. Roughness and curvature (κ_{sigma}) values used for computations are the ones presented in Section
 428 3.2 and 3.3.

429 Different views of the surface can be provided. The first one in Fig.12a is the usual external view, which
 430 corresponds to what can be seen using a conventional 2.5D surface characterization. The area shown is the
 431 same as in Fig.6 and Fig.10. The two other views shown in Fig.12b, are internal views which can be generated
 432 after extracting the surface from the XCT scan. They offer a unique way to identify deep and sharp notches
 433 that would very often be hidden using conventional characterization methods, see the comparison between
 434 Fig.12a and Fig.12b. Once again, this illustrates the interest in characterizing the surface as a 3D free-form
 435 one obtained by XCT.

436 4. Application of the developed methodology to parts with complex geometries

437 In order to test the ability of the methodology developed in this work to characterize complex geometries,
 438 two E-PBF Ti64 architected materials were studied: a gyroid structure and an octet-truss lattice structure.
 439 Both would be impossible to characterize using conventional 2.5D characterization tools and methodologies.
 440

441 4.1. Gyroid structure

442 Fig.13a shows a picture of the studied gyroid. Two local tomography scans [82] were acquired at the
 443 center of the structure. Large artifacts were observed on the XCT scans, which made the use of the presented
 444 threshold for bimodal histograms inappropriate. Otsu's threshold was found to be more efficient in this case.
 445 To examine the influence of voxel size on roughness, curvature, and K_t^* measurements, two distinct voxel
 446 sizes were employed: 5 μm and 10 μm . In either case, roughness and curvature calculations were done using
 447 $\lambda_c = 0.8 \text{ mm}$ and $r_{\text{curv}} = 50 \mu\text{m}$.

448 Fig.13b shows the measured roughness 3D map obtained from the lowest resolution scan. Two magni-
 449 fying windows are also displayed to illustrate a down-skin and an up-skin region. One can clearly notice,
 450 quantitatively, the higher roughness in the down-skin area. The roughness parameters measured for both
 451 voxel sizes are summarized in Tab.3. The average roughness S_a is slightly lower for the lower-resolution
 452 scan, which is consistent since a lower resolution tends to smooth the surface.

453 The higher maximum height S_z and maximum valley depth S_v , are respectively 52 μm and 45 μm higher
 454 for the higher resolution scan, compared with the lower resolution one. Since the difference is roughly the
 455 same for S_z and S_v , it can be concluded in the present case that sharp and deep notches are slightly better
 456 captured using a smaller voxel size. The improvement is less significant for surface features that have positive
 457 height values such as unmelted powder particles.

458 The skewness S_{sk} (= asymmetry) and kurtosis S_{ku} (= sharpness) values are also consistent with this
 459 conclusion. The increase of S_{ku} with a higher resolution means that the surface height distribution contains
 460 more extreme values. The decrease in S_{sk} may also be related to the fact that notches are better taken
 461 into account. Thus, both S_{ku} and S_{sk} suggest that using a smaller voxel size allows for a better capture of
 462 notches, in particular the deepest ones.

Voxel sizes, S_a , S_v and S_z in μm					
Voxel size	S_a	S_v	S_z	S_{sk}	S_{ku}
5	37.3	420	812	0.42	3.6
10	36.6	375	760	0.55	3.1

Table 3: Roughness parameters measured from the gyroid XCT scans with two voxel sizes using $\lambda_c = 0.8\text{ mm}$ and $\lambda_s = 0.05\text{ mm}$. To ensure consistency between the values measured for the two voxel sizes, the parameters were evaluated using only the roughness values present on the surface available in both scans.

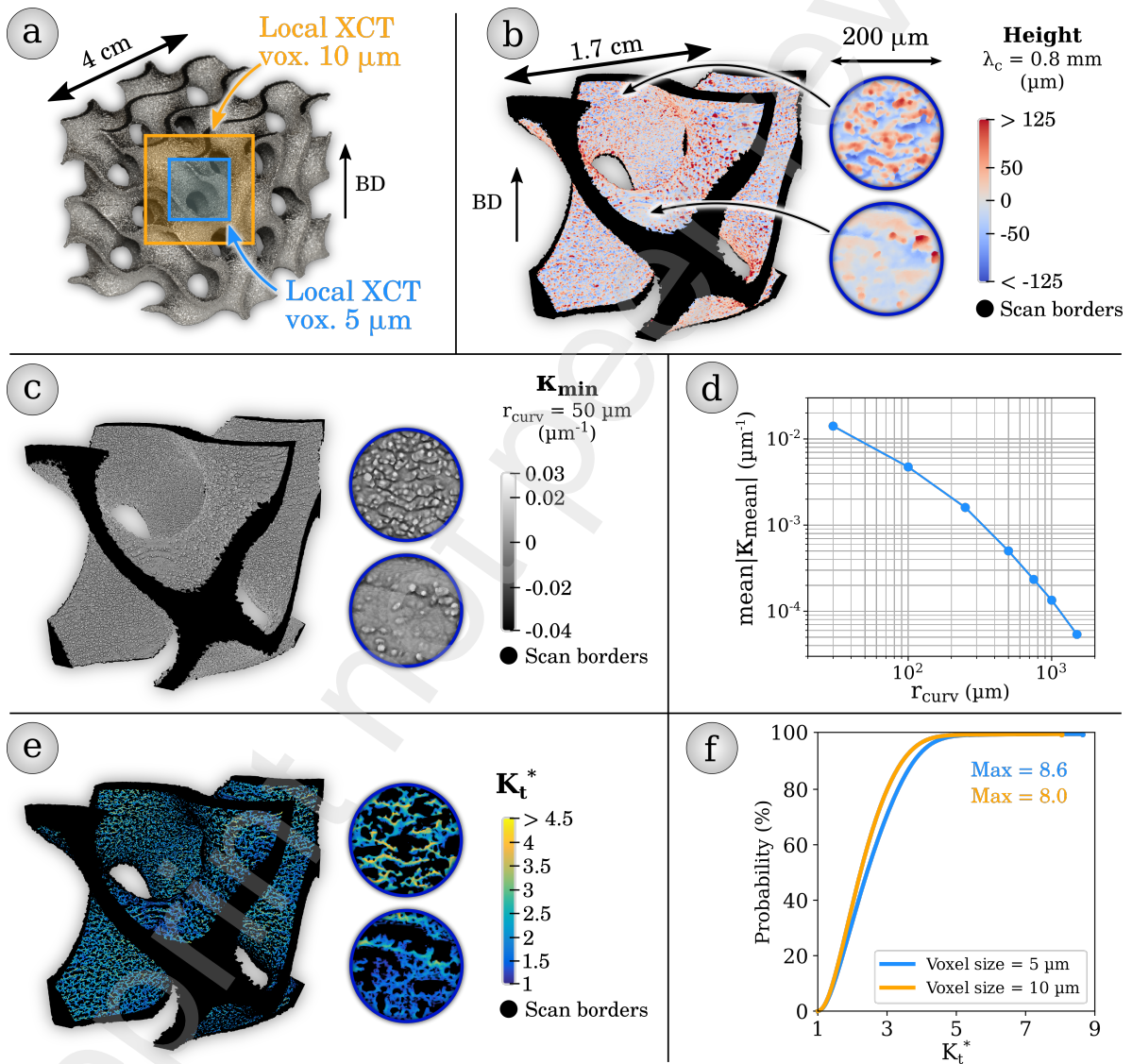


Figure 13: 3D characterization of an E-PBF Ti64 gyroid. The 3D roughness maps shown were obtained from the XCT scan made with a $10\text{ }\mu\text{m}$ voxel size. (a) Picture of the gyroid sample. (b) 3D roughness map with magnifying windows showing a down-skin and an up-skin region ($\lambda_c = 0.8\text{ mm}$ and $\lambda_s = 0.05\text{ mm}$). (c) 3D minimum curvature map with magnifying windows showing a down-skin and an up-skin region ($r_{\text{curv}} = 50\text{ }\mu\text{m}$ and $\lambda_s = 0.05\text{ mm}$). (d) Cumulative distribution function of K_t^* for both voxel sizes. The same area was used for the comparison of both scans.

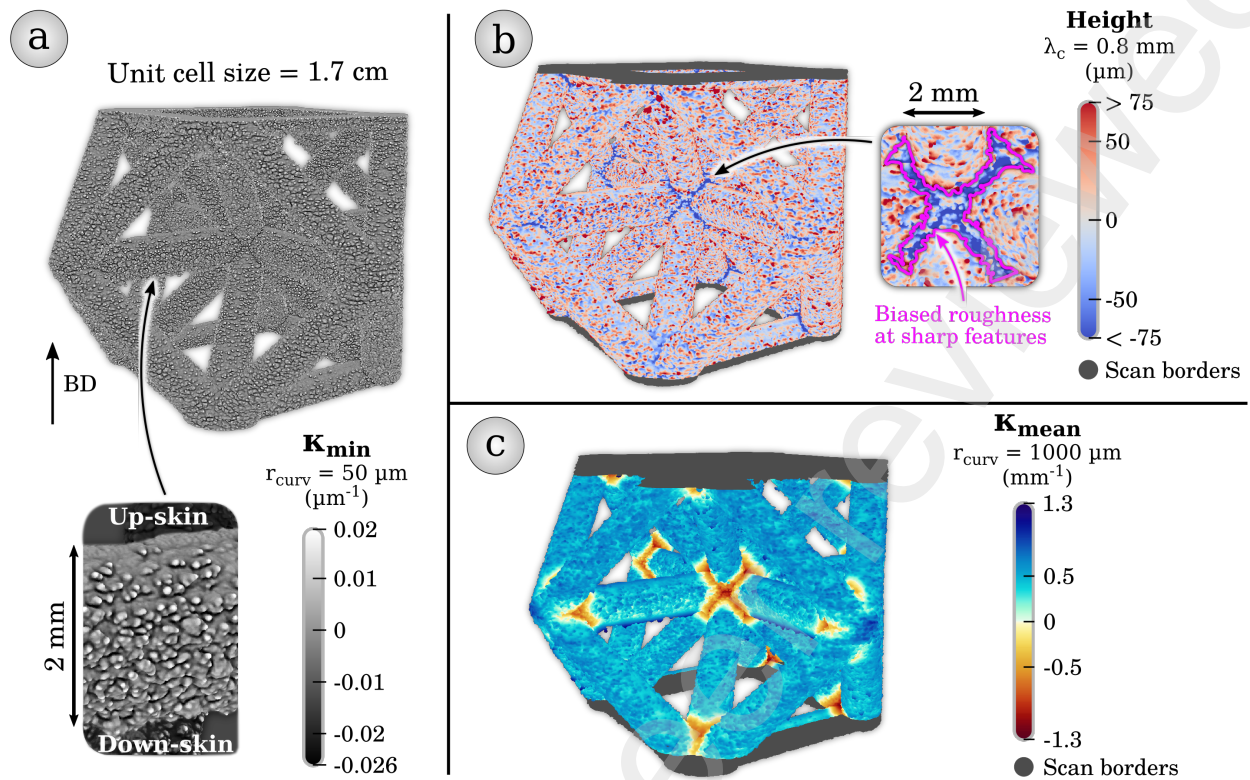


Figure 14: 3D characterization of an E-PBF Ti64 octet-truss lattice structure. (a) 3D minimum curvature map ($r_{curv} = 50 \mu\text{m}$ and $\lambda_S = 0.05 \text{mm}$). (b) 3D roughness map ($\lambda_c = 0.8 \text{mm}$ and $\lambda_S = 0.05 \text{mm}$) with magnifying windows showing the region near the lattice node where roughness measurements are biased. (c) 3D mean curvature map computed at large scale ($r_{curv} = 1000 \mu\text{m}$ and $\lambda_S = 0.05 \text{mm}$). Nodes, where roughness measurements are biased, are clearly identified thanks to their low mean curvature. The region highlighted in purple in b corresponds to the one with a mean curvature lower than -0.4mm^{-1} .

463 Fig.13c shows the 3D κ_{min} map on the same surface as Fig.13b. Fig.13d illustrates how curvature evolves
 464 with respect to the convolution radius r_{curv} . The mean curvature is used here since it is known that it
 465 should equal zero for an ideal gyroid, i.e. with no roughness. The average value across the entire surface
 466 is represented by the average of absolute values $mean|\kappa_{mean}|$, analogous to the role $S_a = mean|height|$ plays
 467 in roughness metrics. As observed in Fig.13d, $mean|\kappa_{mean}|$ tends to zero with increasing r_{curv} values. This is
 468 because a larger r_{curv} measures curvature at a larger scale, corresponding more to the gyroid shape (with
 469 zero mean curvature) than microscopic surface features, which have pronounced curvatures.

470 Finally, Fig.13e-f show the K_t^* measurements derived from roughness and curvature. Note that since
 471 the gyroid could be mechanically loaded in any direction, the minimum curvature is used instead of κ_σ
 472 to compute K_t^* . Fig.13e shows the 3D K_t^* map obtained from the scan performed with a $10 \mu\text{m}$ voxel size.
 473 Meanwhile, the cumulative distribution functions of the K_t^* parameter for both voxel sizes are given in
 474 Fig.13f. The obtained K_t^* values are slightly higher for the $5 \mu\text{m}$ voxel size scan. This can, once again, be
 475 attributed to the better ability at high resolution to properly capture sharp and deep notches.

476 However, for both roughness and K_t^* measurements, the benefits from decreasing the voxel size by a factor
 477 of 2 appear rather limited. The values obtained from the two voxel sizes turn out to be in good agreement.
 478 Considering that a voxel size reduction by a factor of 2 results in an eightfold increase in volume size and
 479 limits the analysis of larger objects, the benefits might not justify the trade-offs in this case.

480 4.2. Octet-truss lattice structure

481 While the gyroid shows the ability to characterize a complex 3D structure, it is a favorable example
 482 regarding the roughness measurement because it does not have sharp features like corners where roughness

483 measurements will tend to be biased. To account for this effect, the second example chosen is an octet-truss
484 lattice structure which, contrary to the gyroid case presents sharp features. Fig.14a shows the κ_{min} 3D map
485 of the octet-truss. Here again, one has a good perception of the volume and surface topography details when
486 the curvature is used for the 3D rendering.

487 Fig.14b shows the 3D roughness map using a cut-off wavelength $\lambda_c = 0.8$ mm. It can be seen that
488 roughness is successfully measured everywhere on the octet-truss lattice, except at nodes where points'
489 height is clearly lower than it should be (see the regions delineated in purple). This shows the limit of the
490 Gaussian filter to derive the reference surface and roughness measurements near sharp features.

491 It is possible to get around this issue by discarding the roughness values in those regions. This can be
492 done manually or with the help of a mean curvature computation. In the case of the octet-truss lattice
493 structure, the mean curvature was measured using the integral invariant approach described in Section 3.3
494 and a large convolution radius of 1 mm, see Fig.14c. It can be seen that nodes are characterized by a very
495 low mean curvature at this scale. For example, the regions delimited in purple in Fig.14b were obtained by
496 thresholding the mean curvature using a manually chosen value of -0.4 mm⁻¹.

497 The limitation of this method is that it does not enable the estimation of roughness at sharp features.
498 Those may, however, be areas of particular interest. For example, it is the case if the aim is to quantify the
499 impact of surface roughness on mechanical properties. Indeed, sharp features will have a stress concentration
500 effect that will add to that due to the presence of surface notches. Even though this problem is complex
501 and has no ideal solution, more advanced smoothing methods such as anisotropic diffusion of normals [59]
502 may be relevant in such cases as a replacement for the conventional Gaussian filter. They are indeed used to
503 smooth surfaces while keeping sharp features of the object's form. This could lead to less biased roughness
504 values at sharp features.

505 Concerning the K_t^* values obtained for complex structures, it is worth noting that the computed values
506 estimate only the stress concentration generated by the surface topography at a micro-scale. For a more
507 complete characterization, one may want to add the contribution of the macroscopic geometry. The latter
508 may be computed using Finite Element Modeling (FEM) on the ideal part geometry. The same calculations
509 could also be used to estimate locally the direction of maximum principal stress. These directions could
510 then be used to compute the curvature instead of using a single direction for the whole part.

511

512 5. Summary

513 In this study, we propose a methodology for the 3D characterization of surface topography using XCT
514 data, focusing on measuring both roughness and 3D curvature. While this methodology has broader appli-
515 cations, we emphasized its usefulness on samples produced by additive manufacturing (E-PBF).

516 Key findings can be summarized as follows:

- 517 • The proposed methodology could effectively account for hidden surface features on surfaces inherited
518 from E-PBF. For example, the 3D method can identify notches that traditional 2.5D techniques would
519 miss.
- 520 • Our method effectively captures roughness and curvature in complex geometries such as architected
521 structures. While the results are encouraging, certain geometric features, like sharp edges, present
522 challenges in roughness assessments. In such instances, more sophisticated metrological tools might
523 offer deeper insights.
- 524 • We have tailored the methodology to make it accessible, even for those unfamiliar with advanced
525 data analysis tools and programming. For example, we deliberately used standard image analysis
526 techniques, such as 3D Gaussian filtering, to extract roughness from the raw surface. This approach
527 can be applied using popular software like ImageJ. With the Gaussian filter being a standard operation
528 for the analysis of 2D and 2.5D roughness, guidelines from ISO standards can be adapted for the
529 presented 3D workflow.
- 530 • We introduced several tools to leverage this 3D characterization in understanding the mechanical im-
531 plications of surface notches. For instance, it was found that the standard Otsu's thresholding missed
532 some of the sharpest notches. We proposed an alternative, the triangle threshold for bimodal his-
533 togram, which yielded better results in this case. Additionally, 3D curvature measurements enable
534 the derivation of curvature in the direction of principal stress, κ_σ , underscoring the mechanical conse-
535 quences of notches aligned perpendicular to the loading direction. Finally, we also proposed a model
536 that integrates roughness and curvature data to compute a parameter, K_t^* , that reflects the stress
537 concentration induced by surface notches.
- 538 • This method is currently applied to investigate the influence of surface roughness on fatigue properties
539 and surface crack initiation mechanisms. This ongoing study focuses on E-PBF and L-PBF Ti64
540 samples, before and after polishing treatments. The findings will be detailed in [43].

541 Acknowledgements

542 This work, conducted at MATEIS and SIMaP laboratories, falls within the framework of the AERO-
543 PRINT project, which received financial support from the Auvergne-Rhône-Alpes Region and the company
544 Dassault Aviation, France. The authors would also like to thank Théo Persenot for providing part of the
545 data used in this paper.

546 Appendix A. 3D Gaussian S-Filter using normalized convolution

547 The following methodology can be used to apply any 3D linear filter on a set of voxels. In particular, it
548 can be used to apply a Gaussian S-filter (or L-filter) to roughness values calculated following the workflow
549 described in Section 3.2. It can be considered as a particular application case of the concept of normalized
550 convolution introduced by Knutsson and Westin [66]. Conversely to a conventional convolution where all
551 voxels are taken into account, normalized convolution can be used to ignore certain voxels. Here, it will
552 be used to ignore background voxels and thus filter only the ones that carry actual information – i.e. the
553 surface voxels that carry roughness values.

554
555 A linear filter is an operation where the value at a given voxel is replaced by a linear combination of
556 the value at the given point and its neighbors. Each neighbor has a specific weight w , i.e. the weight of
557 its contribution to the final filtered value. The matrix assigning the weights for the central voxel and its
558 neighbors is called the filter kernel. For a uniform (= mean) filter, all weights in the kernel will have the
559 same weight. In the case of a Gaussian filter, weights decrease as the distance to the central voxel increases
560 following a Gaussian law, see Fig.A.15. In both cases, weights are generally normalized, meaning the sum
561 of all kernel weights equals 1. For example, this ensures that applying a Gaussian filter to a uniform volume
562 made of 1 will result in a uniform volume made of 1. This is the standard "global" normalization illustrated
563 in Fig.A.15 and employed in common Gaussian filter implementations.

564
565 However, the situation is a bit different when applying a S-filter to a set of surface voxels. In such a case,
566 to compute the filtered value at a given voxel, only neighbor surface voxels should be taken into account
567 instead of all neighbor voxels. The solution would be to explicitly loop over surface voxels only, and never
568 visit background voxels. This can be done in programming languages such as C++. However, this still
569 requires some programming skills, especially to achieve reasonable computation times. Conversely, there are
570 already many efficient implementations of the standard Gaussian filter, including ones accelerated via GPU
571 of FFT computations. The idea here is thus to use such optimized implementations ingeniously to compute
572 indirectly the S-filter.

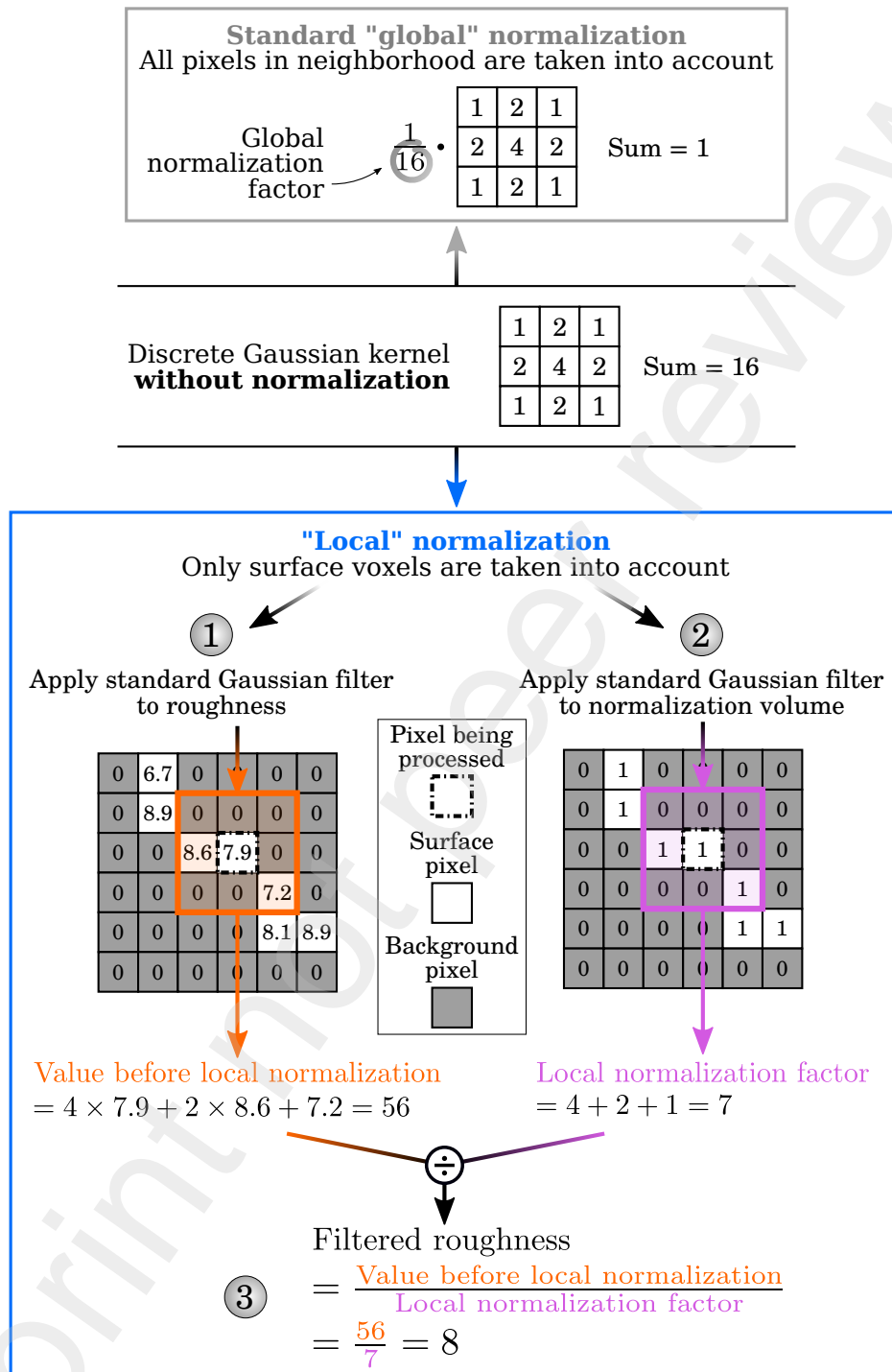


Figure A.15: Workflow proposed for the application of a 3D Gaussian S-filter. All calculations are done using operations on digital volumes, just as the rest of the roughness computation workflow. The example provided in the present figure is restricted to 2D, which means voxels are replaced by pixels. This choice is made to facilitate understanding and visualization, considering the adaptation to a 3D case is straightforward. Note that in steps 1 and 2 of the "local normalization" in Fig.A.15, a non-normalized Gaussian filter is used for the sake of clarity only. The same steps can therefore be followed using a conventional Gaussian filter.

To do so, the first step consists of applying a conventional Gaussian filter to the volume where surface voxels contain roughness values, while background voxels contain 0 – see step 1 in Fig.A.15. Thus, background voxels do not contribute to the final filtered value. Even though, the obtained filter is not properly normalized. Indeed, the sum of the weights of all neighbors that are taken into account (i.e. all neighbor surface voxels) should equal 1. However, this sum will be in general much lower than one, because most neighbor voxels are background ones (equal to 0). To correct this bias, one simply needs to compute the same conventional Gaussian filter to a volume containing 0 at background voxels and 1 at surface voxels, see step 2 in Fig.A.15.

The resulting value at each point is the sum of all the Gaussian kernel weights that effectively come across surface voxels. It can be considered as a "local normalization factor", since by dividing the filtered value obtained in step 1 by this value, we obtain a properly normalized S-filter, see step 3 in Fig.A.15. This method is equivalent to use at each voxel a specific kernel. The latter contains 0 at background voxels, and at other voxels, a weight decreasing according to a Gaussian law with the distance to the central voxel. To be normalized, the sum of all weights must be equal to one. The trick here is to achieve such a (non-linear) computation using only linear filtration steps – i.e. using the same unique kernel for all voxels.

References

- [1] J. Dias Corpa Tardelli, A. C. Duarte Firmino, I. Ferreira, A. Cândido Dos Reis, Influence of the roughness of dental implants obtained by additive manufacturing on osteoblastic adhesion and proliferation: A systematic review, *Heliyon* 8 (2022). URL: <https://linkinghub.elsevier.com/retrieve/pii/S2405844022037938>. doi:10.1016/j.heliyon.2022.e12505.
- [2] R. K. Alla, K. Ginjupalli, N. Upadhya, M. Shamma, R. Krishna, R. Sekhar, Surface Roughness of Implants: A Review, *Trends in Biomaterials & Artificial Organs* 25 (2011) 112–118.
- [3] Y.-T. Jhong, C.-Y. Chao, W.-C. Hung, J.-K. Du, Effects of Various Polishing Techniques on the Surface Characteristics of the Ti-6Al-4V Alloy and on Bacterial Adhesion, *Coatings* 10 (2020). URL: <https://www.mdpi.com/2079-6412/10/11/1057>. doi:10.3390/coatings10111057.
- [4] K. Bohinc, G. Dražić, A. Abram, M. Jevšnik, B. Jeršek, D. Nipič, M. Kurinčič, P. Raspor, Metal surface characteristics dictate bacterial adhesion capacity, *International Journal of Adhesion and Adhesives* 68 (2016) 39–46. URL: <https://linkinghub.elsevier.com/retrieve/pii/S014374961630001X>. doi:10.1016/j.ijadhadh.2016.01.008.
- [5] S. Sneddon, Y. Xu, M. Dixon, D. Rugg, P. Li, D. M. Mulvihill, Sensitivity of material failure to surface roughness: A study on titanium alloys Ti64 and Ti407, *Materials & Design* 200 (2021) 109438. URL: <https://linkinghub.elsevier.com/retrieve/pii/S0264127520309746>. doi:10.1016/j.matdes.2020.109438.
- [6] S. Gürgen, M. C. Kuşhan, S. F. Diltemiz, Fatigue failure in aircraft structural components, in: *Handbook of Materials Failure Analysis with Case Studies from the Aerospace and Automotive Industries*, Elsevier, 2016, pp. 261–277. URL: <https://linkinghub.elsevier.com/retrieve/pii/B9780128009505000132>. doi:10.1016/B978-0-12-800950-5.00013-2.
- [7] A. Toloie, V. Stoilov, D. Northwood, The Relationship Between Surface Roughness and Corrosion, in: *Volume 2B: Advanced Manufacturing*, American Society of Mechanical Engineers, San Diego, California, USA, 2013. URL: <https://asmedigitalcollection.asme.org/IMECE/proceedings/IMECE2013/56192/San%20Diego,%20California,%20USA/260989>. doi:10.1115/IMECE2013-65498.
- [8] T. Persenot, A. Burr, G. Martin, J.-Y. Buffiere, R. Dendievel, E. Maire, Effect of build orientation on the fatigue properties of as-built Electron Beam Melted Ti-6Al-4V alloy, *International Journal of Fatigue* 118 (2019) 65–76. doi:10.1016/j.ijfatigue.2018.08.006.
- [9] L. Deconinck, E. Bernardo Quejido, M. T. Villa Vidaller, E. A. Jäggle, K. Verbeken, T. Depover, The mechanism behind the effect of building orientation and surface roughness on hydrogen embrittlement of laser powder bed fused Ti-6Al-4V, *Additive Manufacturing* 72 (2023). URL: <https://linkinghub.elsevier.com/retrieve/pii/S2214860423002269>. doi:10.1016/j.addma.2023.103613.
- [10] C. de Formanoir, M. Suard, R. Dendievel, G. Martin, S. Godet, Improving the mechanical efficiency of electron beam melted titanium lattice structures by chemical etching, *Additive Manufacturing* 11 (2016) 71–76. URL: <https://linkinghub.elsevier.com/retrieve/pii/S2214860416300847>. doi:10.1016/j.addma.2016.05.001.
- [11] N. Soro, N. Saintier, J. Merzeau, M. Veidt, M. S. Dargusch, Quasi-static and fatigue properties of graded Ti-6Al-4V lattices produced by Laser Powder Bed Fusion (LPBF), *Additive Manufacturing* 37 (2021). URL: <https://linkinghub.elsevier.com/retrieve/pii/S2214860420310253>. doi:10.1016/j.addma.2020.101653.
- [12] N. Sanaei, A. Fatemi, Defects in additive manufactured metals and their effect on fatigue performance: A state-of-the-art review, *Progress in Materials Science* 117 (2021). URL: <https://linkinghub.elsevier.com/retrieve/pii/S0079642520300888>. doi:10.1016/j.pmatsci.2020.100724.
- [13] A. Charles, M. Bayat, A. Elkaseer, L. Thijs, J. H. Hattel, S. Scholz, Elucidation of dross formation in laser powder bed fusion at down-facing surfaces: Phenomenon-oriented multiphysics simulation and experimental validation, *Additive Manufacturing* 50 (2022). URL: <https://linkinghub.elsevier.com/retrieve/pii/S2214860421006989>. doi:10.1016/j.addma.2021.102551.

- 631 [14] I. Mingareev, T. Bonhoff, A. F. El-Sherif, W. Meiners, I. Kelbassa, T. Biermann, M. Richardson, Femtosecond laser
632 post-processing of metal parts produced by laser additive manufacturing, *J. Laser Appl.* 25 (2014) 5.
- 633 [15] M. Hamidi Nasab, S. Romano, D. Gastaldi, S. Beretta, M. Vedani, Combined effect of surface anomalies and volumetric
634 defects on fatigue assessment of AlSi7Mg fabricated via laser powder bed fusion, *Additive Manufacturing* 34 (2020). URL:
635 <https://linkinghub.elsevier.com/retrieve/pii/S2214860419310991>. doi:10.1016/j.addma.2019.100918.
- 636 [16] J. C. Fox, F. Kim, Z. Reese, C. Evans, Complementary use of optical metrology and X-ray computed tomography for
637 surface finish and defect detection in laser powder bed fusion additive manufacturing, *American Society for Precision
638 Engineering* 69 (2018) 195–200.
- 639 [17] A. Townsend, Surface texture metrology for metal additive manufacturing: a review, *Precision Engineering* 46 (2016)
640 34–47.
- 641 [18] U. Ali, Internal surface roughness enhancement of parts made by laser powder-bed fusion additive manufacturing, *Vacuum*
642 177 (2020).
- 643 [19] H. Haitjema, Uncertainty estimation of 2.5-D roughness parameters obtained by mechanical probing, *International
644 Journal of Precision Technology* 3 (2013) 403–412. URL: <http://www.inderscience.com/link.php?id=58260>. doi:10.1504/
645 IJPTECH.2013.058260.
- 646 [20] A. Thompson, Surface texture measurement of metal additively manufactured parts by X-ray computed tomography,
647 Doctoral thesis, University of Nottingham, 2018.
- 648 [21] X. J. Jiang, P. J. Scott, *Advanced metrology: freeform surfaces*, Academic Press, London, 2020.
- 649 [22] H. S. Abdul-Rahman, J. Jiang, P. J. Scott, A Gaussian-like Filtering algorithm for Freeform Surfaces Represented by
650 Triangular Meshes (2013). URL: <http://rgdoi.net/10.13140/RG.2.1.4443.0327>. doi:10.13140/RG.2.1.4443.0327, publisher:
651 Unpublished.
- 652 [23] R. Wang, A. C. Law, D. Garcia, S. Yang, Z. Kong, Development of structured light 3D-scanner with high spatial
653 resolution and its applications for additive manufacturing quality assurance, *The International Journal of Advanced
654 Manufacturing Technology* 117 (2021) 845–862. URL: <https://link.springer.com/10.1007/s00170-021-07780-2>. doi:10.1007/
655 s00170-021-07780-2.
- 656 [24] M. Shahpaski, L. R. Sapaico, S. Süssstrunk, Surface roughness estimation using structured light projection, *Elec-
657 tronic Imaging* 33 (2021). URL: <https://library.imaging.org/ei/articles/33/5/art00005>. doi:10.2352/ISSN.2470-1173.2021.
658 5.MAAP-139.
- 659 [25] S. Lou, L. Pagani, W. Zeng, M. U. Ghorri, X. Jiang, P. J. Scott, Surface texture evaluation of additively manufactured
660 metallic cellular scaffolds for acetabular implants using X-ray computed tomography, *Bio-Design and Manufacturing* 2
661 (2019) 55–64. URL: <http://link.springer.com/10.1007/s42242-019-00042-x>. doi:10.1007/s42242-019-00042-x.
- 662 [26] F. Zanini, L. Pagani, E. Savio, S. Carmignato, Characterisation of additively manufactured metal surfaces by means
663 of X-ray computed tomography and generalised surface texture parameters, *CIRP Annals* 68 (2019) 515–518. URL:
664 <https://linkinghub.elsevier.com/retrieve/pii/S0007850619301039>. doi:10.1016/j.cirp.2019.04.074.
- 665 [27] M. Grazia Guerra, F. Lavecchia, Measurement of additively manufactured freeform artefacts: The influence of surface
666 texture on measurements carried out with optical techniques, *Measurement* 209 (2023). URL: <https://linkinghub.elsevier.com/retrieve/pii/S0263224123001045>. doi:10.1016/j.measurement.2023.112540.
- 667 [28] J. W. McBride, K. J. Cross, The surface area and localised 3D roughness of a highly structured surface using X-Ray
668 Computed tomography (XCT), *Metrology Letters* (2020).
- 669 [29] L. Pagani, S. Lou, W. Zeng, X. Jiang, P. J. Scott, Effect of the form estimation on the areal texture parameters for X-ray
670 computed tomography measurement, *Proc iCT 2018* (2018).
- 671 [30] G. Kerckhofs, G. Pyka, M. Moesen, J. Schrooten, M. Wevers, High-resolution micro-CT as a tool for 3D surface roughness
672 measurement of 3D additive manufactured porous structures, *Proc iCT* (2012).
- 673 [31] J. J. Lifton, Y. Liu, Z. J. Tan, B. Mutiargo, X. Q. Goh, A. A. Malcolm, Internal surface roughness measurement
674 of metal additively manufactured samples via x-ray CT: the influence of surrounding material thickness, *Surface
675 Topography: Metrology and Properties* 9 (2021). URL: <https://iopscience.iop.org/article/10.1088/2051-672X/ac0e7c>.
676 doi:10.1088/2051-672X/ac0e7c.
- 677 [32] C. Inglis, Stresses in plates due to the presence of cracks and sharp corners, *Spie Milestone series MS 137* (1913) 3–17.
- 678 [33] H. Neuber, *Theory of notch stresses: principles for exact calculation of strength with reference to structural form and
679 material*, 1958.
- 680 [34] D. Arola, M. Ramulu, An Examination of the Effects from Surface Texture on the Strength of Fiber Reinforced Plastics,
681 *Journal of Composite Materials* 33 (1999) 102–123. URL: <http://journals.sagepub.com/doi/10.1177/002199839903300201>.
682 doi:10.1177/002199839903300201.
- 683 [35] S. Lee, B. Rasoolian, D. F. Silva, J. W. Pegues, N. Shamsaei, Surface Roughness Parameter and Modeling for Fatigue
684 Behavior of Additive Manufactured Parts: A Non-destructive Data-driven Approach, *Additive Manufacturing* 46 (2021).
685 URL: <https://linkinghub.elsevier.com/retrieve/pii/S2214860421002591>. doi:10.1016/j.addma.2021.102094.
- 686 [36] S. McKelvey, A. Fatemi, Surface finish effect on fatigue behavior of forged steel, *International Journal of Fatigue* 36 (2012)
687 130–145. URL: <https://linkinghub.elsevier.com/retrieve/pii/S0142112311002180>. doi:10.1016/j.ijfatigue.2011.08.008.
- 688 [37] A. Cellier, F. Chalon, V. Grimal-Perrigouas, D. Bonhoure, R. Leroy, Effects of Cutting Angles in Ti-6al-4v Milling Process
689 on Surface Integrity: Influence of Roughness and Residual Stresses on Fatigue Limit, *Machining Science and Technology* 18
690 (2014) 565–584. URL: <http://www.tandfonline.com/doi/abs/10.1080/10910344.2014.955369>. doi:10.1080/10910344.2014.
691 955369.
- 692 [38] D. Arola, C. Williams, Estimating the fatigue stress concentration factor of machined surfaces, *International Jour-
693 nal of Fatigue* 24 (2002) 923–930. URL: <https://linkinghub.elsevier.com/retrieve/pii/S0142112302000129>. doi:10.1016/
694 S0142-1123(02)00012-9.
- 695

- 696 [39] F. Quan, Z. Chen, H. Ye, C. Cui, Y. Cui, Study of the effect of surface roughness on fatigue strength of GH4169 based
697 on indirect evaluation of the notch root radius, *International Journal of Fatigue* 152 (2021). URL: <https://linkinghub.elsevier.com/retrieve/pii/S0142112321002991>. doi:10.1016/j.ijfatigue.2021.106440.
- 698 [40] V. Mereuta, M. Buciumeanu, L. Palaghian, 3D Roughness Parameters as Factors in Determining the Evolution of
699 Effective Stress Concentration Factors in Fatigue Processes, *Applied Mechanics and Materials* 248 (2012) 504–510. URL:
700 <https://www.scientific.net/AMM.248.504>. doi:10.4028/www.scientific.net/AMM.248.504.
- 701 [41] V.-D. Le, E. Pessard, F. Morel, S. Prigent, Effect of the surface roughness on the high cycle fatigue behaviour of Ti-6Al-4V
702 alloy obtained by additive manufacturing process, *Engineering Integrity* 53 (2021).
- 703 [42] S. Pomberger, M. Stoschka, R. Aigner, M. Leitner, R. Ehart, Areal fatigue strength assessment of cast alu-
704 minium surface layers, *International Journal of Fatigue* 133 (2020). URL: <https://linkinghub.elsevier.com/retrieve/pii/S0142112319305274>. doi:10.1016/j.ijfatigue.2019.105423.
- 705 [43] F. Steinhilber, Influence of surface integrity on the fatigue properties of L-PBF Ti64: A 3D investigation by X-ray
706 tomography, Doctoral thesis, Université de Lyon, Lyon, 2024.
- 707 [44] T. Persenot, Fatigue of Ti-6Al-4V thin parts made by electron beam melting, Doctoral thesis, Université de Lyon, Lyon,
708 2018.
- 709 [45] A. H. Schoen, Infinite periodic minimal surfaces without self-intersections, Technical Report D-5541, NASA, 1970.
- 710 [46] L. Yang, C. Yan, W. Cao, Z. Liu, B. Song, S. Wen, C. Zhang, Y. Shi, S. Yang, Compression–compression fatigue behaviour
711 of gyroid-type triply periodic minimal surface porous structures fabricated by selective laser melting, *Acta Materialia* 181
712 (2019) 49–66. URL: <https://linkinghub.elsevier.com/retrieve/pii/S1359645419306329>. doi:10.1016/j.actamat.2019.09.042.
- 713 [47] L. A. Feldkamp, L. C. Davis, J. W. Kress, Practical cone-beam algorithm, *Journal of the Optical Society of America A* 1
714 (1984). URL: <https://opg.optica.org/abstract.cfm?URI=josa-a-1-6-612>. doi:10.1364/JOSAA.1.000612.
- 715 [48] P. Jain, V. Tyagi, A survey of edge-preserving image denoising methods, *Information Systems Frontiers* 18 (2016) 159–170.
716 URL: <http://link.springer.com/10.1007/s10796-014-9527-0>. doi:10.1007/s10796-014-9527-0.
- 717 [49] N. Otsu, A Threshold Selection Method from Gray-Level Histograms, *IEEE Transactions on Systems, Man, and Cyber-*
718 *netics* (1979).
- 719 [50] N. Vanderesse, P. Bocher, N. Nuño, A. Yáñez, L. A. Hof, On the characterization of roughness and geometrical irregularities
720 of additively manufactured single titanium-alloy struts, *Additive Manufacturing* 54 (2022). URL: <https://linkinghub.elsevier.com/retrieve/pii/S221486042200135X>. doi:10.1016/j.addma.2022.102731.
- 721 [51] G. W. Zack, W. E. Rogers, S. A. Latt, Automatic measurement of sister chromatid exchange frequency., *Journal of*
722 *Histochemistry & Cytochemistry* 25 (1977) 741–753. URL: <http://journals.sagepub.com/doi/10.1177/25.7.70454>. doi:10.
723 1177/25.7.70454.
- 724 [52] S. Pomberger, M. Stoschka, M. Leitner, Cast surface texture characterisation via areal roughness, *Precision Engineering* 60
725 (2019) 465–481. URL: <https://linkinghub.elsevier.com/retrieve/pii/S0141635919302818>. doi:10.1016/j.precisioneng.2019.
726 09.007.
- 727 [53] International Organisation for Standardization, ISO 25178-3:2012 Geometrical product specifications (GPS) - Surface
728 texture: Areal - Part 3: Specification operators, 2012.
- 729 [54] E. Savio, L. De Chiffre, R. Schmitt, Metrology of freeform shaped parts, *CIRP Annals* 56 (2007) 810–835. URL:
730 <https://linkinghub.elsevier.com/retrieve/pii/S0007850607001588>. doi:10.1016/j.cirp.2007.10.008.
- 731 [55] X. Jiang, X. Zhang, P. J. Scott, Template matching of freeform surfaces based on orthogonal distance fitting for precision
732 metrology, *Measurement Science and Technology* 21 (2010). URL: <https://iopscience.iop.org/article/10.1088/0957-0233/21/4/045101>.
733 doi:10.1088/0957-0233/21/4/045101.
- 734 [56] H. Villarraga-Gómez, C. M. Peitsch, A. Ramsey, S. T. Smith, THE ROLE OF COMPUTED TOMOGRAPHY IN
735 ADDITIVE MANUFACTURING 69 (2018).
- 736 [57] S. Lou, W.-H. Zeng, X.-Q. Jiang, P. J. Scott, Robust Filtration Techniques in Geometrical Metrology and Their Com-
737 parison, *International Journal of Automation and Computing* (2013) 1–8.
- 738 [58] X. Jiang, P. Cooper, P. J. Scott, Freeform surface filtering using the diffusion equation, *Proceedings of the Royal Society*
739 *A: Mathematical, Physical and Engineering Sciences* 467 (2011) 841–859. URL: <https://royalsocietypublishing.org/doi/10.1098/rspa.2010.0307>.
740 doi:10.1098/rspa.2010.0307.
- 741 [59] T. Tasdizen, R. Whitaker, P. Burchard, S. Osher, Geometric surface smoothing via anisotropic diffusion of normals, *IEEE*,
742 Boston, MA, USA, 2002, pp. 125–132. URL: <http://ieeexplore.ieee.org/document/1183766/>. doi:10.1109/VISUAL.2002.
743 1183766.
- 744 [60] X. J. Jiang, P. J. Scott, Free-form surface filtering using wavelets and multiscale decomposition, in: *Advanced Metrol-*
745 *ogy*, Elsevier, 2020, pp. 195–246. URL: <https://linkinghub.elsevier.com/retrieve/pii/B9780128218150000095>. doi:10.1016/
746 B978-0-12-821815-0.00009-5.
- 747 [61] F. Steinhilber, 3D roughness computation from XCT data - Data and Python & ImageJ implementations, 2023. doi:10.
748 5281/zenodo.10036352.
- 749 [62] S. Lou, X. Jiang, P. J. Scott, Geometric computation theory for morphological filtering on freeform surfaces, *Proceedings*
750 *of the Royal Society A: Mathematical, Physical and Engineering Sciences* (2013). URL: <https://royalsocietypublishing.org/doi/10.1098/rspa.2013.0150>.
751 doi:10.1098/rspa.2013.0150.
- 752 [63] International Organisation for Standardization, ISO 16610-60:2015 Geometrical product specification (GPS) - Filtration -
753 Part 60: Linear areal filters - Basic concepts, 2015.
- 754 [64] S. Lou, X. Jiang, W. Sun, W. Zeng, L. Pagani, P. Scott, Characterisation methods for powder bed fusion processed surface
755 topography, *Precision Engineering* 57 (2019) 1–15. URL: <https://linkinghub.elsevier.com/retrieve/pii/S0141635918300345>.
756 doi:10.1016/j.precisioneng.2018.09.007.
- 757 [65] M. Vetterli, M. Schmid, K. Wegener, Comprehensive investigation of surface characterization for laser sintered parts, in:

- DDMC 2014 : Fraunhofer Direct Digital Manufacturing Conference : proceedings, 2014. URL: <http://hdl.handle.net/20.500.11850/97466>. doi:10.3929/ETHZ-A-010357719, artwork Size: 6 p. Medium: application/pdf Publisher: ETH Zurich.
- [66] H. Knutsson, C.-F. Westin, Normalized and differential convolution, in: Proceedings of IEEE Conference on Computer Vision and Pattern Recognition, IEEE Comput. Soc. Press, New York, NY, USA, 1993, pp. 515–523. URL: <http://ieeexplore.ieee.org/document/341081/>. doi:10.1109/CVPR.1993.341081.
- [67] International Organisation for Standardization, ISO 16610-28:2016 Geometrical product specifications (GPS) — Filtration — Part 28: Profile filters: End effects, 2016.
- [68] D. Janecki, Edge effect elimination in the recursive implementation of Gaussian filters, Precision Engineering 36 (2012) 128–136. URL: <https://linkinghub.elsevier.com/retrieve/pii/S0141635911001346>. doi:10.1016/j.precisioneng.2011.08.001.
- [69] G. Taubin, Estimating the tensor of curvature of a surface from a polyhedral approximation, in: Proceedings of IEEE International Conference on Computer Vision, Cambridge, MA, USA, 1995, pp. 902–907. URL: <http://ieeexplore.ieee.org/document/466840/>. doi:10.1109/ICCV.1995.466840.
- [70] F. Cazals, M. Pouget, Estimating differential quantities using polynomial fitting of osculating jets, Computer Aided Geometric Design 22 (2005) 121–146. URL: <https://linkinghub.elsevier.com/retrieve/pii/S016783960400113X>. doi:10.1016/j.cagd.2004.09.004.
- [71] J.-O. Lachaud, D. Coeurjolly, J. Levallois, Robust and Convergent Curvature and Normal Estimators with Digital Integral Invariants, in: L. Najman, P. Romon (Eds.), Modern Approaches to Discrete Curvature, Springer International Publishing, Cham, 2017, pp. 293–348. URL: http://link.springer.com/10.1007/978-3-319-58002-9_9.
- [72] D. Coeurjolly, J.-O. Lachaud, J. Levallois, Multigrid convergent principal curvature estimators in digital geometry, Computer Vision and Image Understanding 129 (2014) 27–41. URL: <https://linkinghub.elsevier.com/retrieve/pii/S1077314214001003>. doi:10.1016/j.cviu.2014.04.013.
- [73] DGTal Team, DGTal, 2022. URL: <https://dgtal.org/>.
- [74] M. J. Blunt, Q. Lin, T. Akai, B. Bijeljic, A thermodynamically consistent characterization of wettability in porous media using high-resolution imaging, Journal of Colloid and Interface Science 552 (2019) 59–65. URL: <https://linkinghub.elsevier.com/retrieve/pii/S0021979719305648>. doi:10.1016/j.jcis.2019.05.026.
- [75] L. Yuan, S. Ding, C. Wen, Additive manufacturing technology for porous metal implant applications and triple minimal surface structures: A review, Bioactive Materials 4 (2019) 56–70. URL: <https://linkinghub.elsevier.com/retrieve/pii/S2452199X18300768>. doi:10.1016/j.bioactmat.2018.12.003.
- [76] M. Tilton, A. Borjali, J. C. Griffis, K. M. Varadarajan, G. P. Manogharan, Fatigue properties of Ti-6Al-4V TPMS scaffolds fabricated via laser powder bed fusion, Manufacturing Letters 37 (2023) 32–38. URL: <https://linkinghub.elsevier.com/retrieve/pii/S2213846323000317>. doi:10.1016/j.mfglet.2023.06.005.
- [77] C. Polley, W. Radlof, F. Hauschulz, C. Benz, M. Sander, H. Seitz, Morphological and mechanical characterisation of three-dimensional gyroid structures fabricated by electron beam melting for the use as a porous biomaterial, Journal of the Mechanical Behavior of Biomedical Materials 125 (2022). URL: <https://linkinghub.elsevier.com/retrieve/pii/S1751616121005166>. doi:10.1016/j.jmbbm.2021.104882.
- [78] D. Khrapov, M. Kozadayeva, K. Manabaev, A. Panin, W. Sjöström, A. Koptyug, T. Mishurova, S. Evsevlev, D. Meinel, G. Bruno, D. Cheneler, R. Surmenev, M. Surmeneva, Different Approaches for Manufacturing Ti-6Al-4V Alloy with Triply Periodic Minimal Surface Sheet-Based Structures by Electron Beam Melting, Materials 14 (2021). URL: <https://www.mdpi.com/1996-1944/14/17/4912>. doi:10.3390/ma14174912.
- [79] L. Zhang, S. Feih, S. Daynes, S. Chang, M. Y. Wang, J. Wei, W. F. Lu, Energy absorption characteristics of metallic triply periodic minimal surface sheet structures under compressive loading, Additive Manufacturing 23 (2018) 505–515. URL: <https://linkinghub.elsevier.com/retrieve/pii/S2214860418304688>. doi:10.1016/j.addma.2018.08.007.
- [80] C. A. Kantzos, R. W. Cunningham, V. Tari, A. D. Rollett, Characterization of metal additive manufacturing surfaces using synchrotron X-ray CT and micromechanical modeling, Computational Mechanics 61 (2018) 575–580. doi:10.1007/s00466-017-1531-z.
- [81] A. du Plessis, E. Macdonald, Hot isostatic pressing in metal additive manufacturing_ X-ray tomography reveals details of pore closure, Additive Manufacturing 34 (2020).
- [82] S. R. Stock, Recent advances in X-ray microtomography applied to materials, International Materials Reviews 53 (2008) 129–181. URL: <http://www.tandfonline.com/doi/full/10.1179/174328008X277803>. doi:10.1179/174328008X277803.